

UNIVERSITÀ DEGLI STUDI DI TRIESTE

XXXII CICLO DEL DOTTORATO DI RICERCA IN
INGEGNERIA INDUSTRIALE E DELL'INFORMAZIONE

CONCENTRATED WINDING
ELECTRICAL MACHINE MODELLING,
DESIGN AND OPTIMIZATION

ING-IND/32

CONVERTITORI, MACCHINE E AZIONAMENTI ELETTRICI

Author:

Nicola BARBINI

Supervisor:

Prof. Alberto TESSAROLO

Coordinator:

Prof. Fulvio BABICH

ANNO ACCADEMICO

2018 – 2019

Abstract

Concentrated Winding Electrical Machine Modelling, Design and Optimization

Over the last few years, fractional slot concentrated winding (FSCW) electrical machines have received increasing attention mainly due to their characteristics of low manufacturing cost and short end-coil dimensions. Conversely, if compared with traditional distributed winding, FSCWs are known to produce large space harmonics in the air-gap, which may lead to several issues such as eddy current losses and unbalanced magnetic pull (UMP).

In this thesis, the possibility is investigated of optimizing FSCWs to minimize magnet losses and UMP issues. FSCW with unconventional slot-pole combinations are introduced and analysed, based on a quadratic programming procedure.

The developed theory is applied to the design and analysis of a test machine prototype.

Modellizzazione, progettazione e ottimizzazione di macchine elettriche ad avvolgimenti concentrati

Negli ultimi anni, le macchine elettriche ad avvolgimenti concentrati hanno ricevuto sempre più attenzioni principalmente per le loro caratteristiche di un basso costo di produzione e di un ridotto ingombro delle testate. Per contro, rispetto alle più diffuse macchine ad avvolgimenti distribuiti, sono note per avere un forte contenuto armonico spaziale che può dare origine a vari inconvenienti tra cui l'aumento delle perdite nei magneti e forze radiali indesiderate tra rotore e statore (UMP).

Nella presente tesi viene analizzata la possibilità di ottimizzare gli avvolgimenti concentrati a cave frazionarie (FSCW) per minimizzare le perdite nei magneti e l'UMP. Gli FSCW non convenzionali Vengono introdotti, analizzati ed ottimizzati tramite ottimizzazione quadratica. La teoria sviluppata viene applicata alla progettazione ed analisi di un prototipo di prova.

Contents

Abstract	i
Notation	viii
Introduction	1
1 FSCW and Extended-FSCW formalization	5
1.1 Topolgy description	5
1.2 Stator contribution to air gap harmonic content	6
1.2.1 Basic definitions	6
1.2.2 Modelling space harmonics	9
1.2.3 Mutual dependence of space harmonics	14
1.2.4 Winding factor computation	20
1.3 SPM rotor contribution to air gap harmonic content	22
2 FSCW air gap harmonic content optimization	27
2.1 Constraints	29
2.2 Objective function	32
2.3 Fundamental harmonic maximization	32
2.3.1 Winding selection	36
2.4 Permanent magnet losses minimization	37
2.5 Unbalanced magnetic pull analysis and minimization	44
2.5.1 Magnetic interaction between stator and rotor	45
2.5.2 Harmonics causing dynamic UMP	46
2.5.3 Rotational symmetry	56
2.5.4 Application to a case study	58
3 Study and implementation of an unconventional FSCW	67
3.1 Machine specifications and requirements	68
3.2 Rotor	68
3.3 Stator	69
3.4 Unconventional FSCW choice	72

3.5	Mechanical design	75
3.6	Measurements	78
	Conclusion	81

List of Figures

1.1	Phasor representation of three phase system: (a) classical and (b) dummy	7
1.2	MMF along the gap angular coordinate θ at time t due to the sole tooth 0 contribution	9
1.3	The MMF along the air gap angular coordinate θ for the conventional 9-8 configuration with $\omega t = 0.2$. In green the actual wave-shape, in red its fundamental ($n = p$).	11
1.4	Amplitude of the harmonics produced by the star-of-slots winding in a conventional 9 – 8 configuration, in red the harmonics rotating anticlockwise like the fundamental, in blue the harmonics rotating clockwise.	13
1.5	Amplitudes of the harmonics for a 9 teeth, 8 pole conventional configuration, in red the harmonics rotating anticlockwise as the fundamental, in blue the harmonics rotating clockwise, in green the function $f(p, n)$	17
1.6	Amplitudes of the harmonics for a 9 – 8 conventional configuration. The function $f(p, n)$ (in green) highlights the members of the family H_p . The function $f(7, n)$ (in purple) highlights the members of the family H_7	19
1.7	MMF due to the surface magnets, where θ is rotor referenced angular position. τ_p pole pitch, k_{mag} magnet width to pole pitch ratio and h_{mag} magnet height.	23
1.8	Normalized $\text{rect}_N(\alpha)$ on its 2π period	24
1.9	$\text{rect}(\theta_R)$ representation with arbitrary number of p pole pairs, where τ_p is the pole pitch and τ_{mag} is the angular magnet width	24

2.1	Example on a per-unit base of a Pareto curve obtained from the fundamental maximization (highlighted by ○) and gradually reducing the fundamental to allow the losses minimization	39
2.2	Representation of a series of linear lower bound optimizations whose envelope coincides with a quadratic lower bound optimization	40
2.3	Losses (red) ratio between losses and the square of the fundamental (blue)	41
2.4	Reduction of the harmonics causing losses on the 9 – 8 configuration, (a) and (c) classic notation winding matrix, (b) and (d) spectra	42
2.5	Amplitudes of the harmonics for the conventional 6 – 4 configuration, in red the harmonics rotating anticlockwise as the fundamental, in blue the harmonics rotating clockwise.	50
2.6	Amplitude of the harmonics for the conventional 9 – 8 configuration, in red the harmonics rotating anticlockwise as the fundamental, in blue the harmonics rotating clockwise.	50
2.7	Comparison between spectra of repeated configurations in order to achieve rotational symmetry	57
2.8	Data used for the 21 – 16 configuration FEA simulation	58
2.9	Spectrum and pull trajectory of a star-of-slots winding applied to 21 – 16 configuration	60
2.10	UMP relative variation iterating the 7 th harmonic minimization. in abscissa the iteration step, corresponding to a fundamental decrease of 0.1%	61
2.11	Relative UMP trajectories for a selection of indexes. The axes scales have been modified in accordance to the UMP module	63
2.12	Comparison between (a) star-of-slots and (b) optimized 21 – 16 configuration spectrum, the increased harmonics are highlighted by the marking changing from green to orange	64
3.1	Concept design of the sailing boat hub-less motor-generator	67
3.2	Half section of the 24 poles rotor	69

3.3	Schematic of the four sections of the machine fed by the four converters	70
3.4	Half section of the 24 poles rotor coupled with the 28 teeth stator	71
3.5	Cogging torque obtained by FEA simulation on the 28 – 24 configuration	72
3.6	Half section of the 28 – 24 configuration with the winding representation	73
3.7	Amplitude of the harmonics for the 28 – 24 configuration, in red the harmonics rotating anticlockwise as the fundamental, in blue the harmonics rotating clockwise.	74
3.8	Half section of the 28 – 24 configuration. the winding colours are related to the current density, the flux lines are represented in red	74
3.9	Torque obtained by a 15A FEA simulation on the 28 – 24 configuration	75
3.10	Section of the sleeved machine the sleeve is highlighted in yellow	76
3.11	Second design of the machine the ball bearing and the hydraulic sealing are shown	76
3.12	Section of the final machine with the cam rollers	77
3.13	Rotor of the prototype	78
3.14	Rotor of the prototype	79
3.15	Test setup	80
3.16	Comparison:	
	ooo test measurements — FEA simulation	80

List of Tables

1	Font types	viii
2	Acronyms	viii
3	Symbols	ix
1.1	(b) Highlighted in blue, example of winding matrix W using dummy phases. (a) beside (highlighted in yellow) its correspondent representation using classic phases. The column index l is relative to the dummy phase, the row index k is relative to the tooth	8
2.1	Example of winding matrix W (highlighted in blue), obtained for the 5 – 4 configuration with $L = 3$	34
2.2	Rounded winding matrix W (highlighted in blue), obtained for the 5 – 4 configuration with $L = 3$	35
2.3	Classic phase notation of the winding matrix (highlighted in yellow), equivalent to Tab. 2.2	35
2.4	Winding factor, obtained for various $Z - 2p$ combinations and three phases ($L = 3$), only the values for which $\frac{1}{4} < q < \frac{1}{2}$ are shown, unconventional configurations are shaded.	37
2.5	Specific losses expressed in mW/mm ³ calculated for various $Z - 2p$ combinations. The unconventional configurations are shaded.	44
2.6	UMP analysis for various combinations of $Z - 2p$. “0” indicates null UMP, “X” indicates that there is UMP that cannot be changed by the winding, “✓” indicates that there is UMP that can be changed modifying the winding. The unconventional configurations are shaded, highlighted in yellow the 21 – 16 combination	52

2.7	Specific UMP, obtained for various $Z - 2p$ combinations, unconventional configurations are shaded, the conventional 21 – 16 is highlighted in yellow and ✓ indicates the configurations for which the UMP can be reduced.	55
2.8	Data used for the 21 – 16 configuration FEA simulation .	59
3.1	Winding matrix used for each 7 – 6 section of the 28 – 24 configuration, $N_t = 60$	73

Notation

Table 1: Font types

Entity	Font type	Example
scalar variables	italic	x
vectors, matrices	up and bold	\mathbf{v}, \mathbf{M}
operators	up	$\sin(\cdot)$
scalar functions	italic	$f(\cdot)$
vectorial functions	italic and bold	$\mathbf{f}(\cdot)$
units	up	$25^\circ\text{C}, \text{J mol}^{-1}$
constants	up	e
complex values	bar	\bar{z}

Table 2: Acronyms

Acronym	meaning
FEA	Finite Element Analysis
FSCW	Fractional Slot Concentrated Winding
IPM	Internal Permanent Magnet
MMF	MagnetoMotive Force
PM	Permanent Magnet
SPM	Surface Permanent Magnet
UMP	Unbalanced Magnetic Pull

Table 3: Symbols

symbol	meaning	page
e	Euler constant	
$\bar{\mathbf{e}}(\theta, t)$	space-time row vector	13
$\bar{\mathbf{i}}$	current phasor column vector	7
j	imaginary unit	
k	tooth index	
l	dummy phase index	
L	number of actual phases	5
LB	Lower Bound	32
\bar{m}_n^\oplus	MMF space harmonic phasor	12
M	magneto-motive force	
n	space harmonic index	
N_t	maximum turns around one tooth	
p	number of pole pairs	5
q	number slots per pole per phase	5
\mathbf{s}_n	selection row vector	13
$\bar{\mathbf{S}}^\oplus$	harmonic extraction matrix	12
t	time	
\mathbf{v}_n^\oplus	harmonic extraction vector	28
\mathbf{W}	winding matrix	8
\mathbf{w}	winding column vector	28
Z	number of teeth (or slots)	5
\mathfrak{C}	constraints	32
\mathfrak{F}	objective function	38
θ	angular position referred to the stator	8
θ_R	angular position referred to the rotor	22
κ_{wn}^\oplus	winding factor of the n^{th} harmonic	20
R_R	rotor iron radius	43
R_{mag}	outer magnet surface radius	43
R_S	stator bore radius	43

Introduction

Over the last few years, Fractional Slot Concentrated Winding (FSCW) electrical machines have gained increasing popularity [1] mainly because of their simple manufacturing and modularity [2], their short end coils [3] and fault tolerance features [4]. Conversely, if compared with traditional distributed windings, FSCWs are known to produce a high spatial harmonic content in the air-gap field, which may lead to several issues such as higher losses [5] [6], undesired unbalanced magnetic pull (UMP), vibrations [7] [8] [9] and torque ripple [10] [11].

Among the FSCW variants, the dual layer one (with a single coil for each tooth) with an arrangement of the winding determined by the star of slots algorithm is the most common choice [12]. The star of slots method (when applicable) guarantees the symmetry of the winding and the maximum fundamental amplitude. It is so widely adopted, that its applicability constraints, involving the slot-pole configuration, are commonly regarded as a feasibility constraint for any FSCW topology [13]. In this work it will be shown that the configurations for which the star of slots is applicable is only a subset of the possible configurations featuring symmetry and high winding factor. The slot-pole configurations for which the star of slots can be applied will be referred to as “conventional”, while the others will be defined as “unconventional”.

In this thesis the cited topics are addressed as follows.

In Chapter 1, an analytical method for the harmonic content evaluation of a FSCW is presented, starting with the definition of a mathematical framework for a generic multi-phase FSCW topology, to get to the prediction of its space harmonic spectrum. The harmonic spectrum is eventually examined to derive the winding factor and to analyse the mutual dependence among the harmonics.

In Chapter 2, the formalism developed in chapter 1 is used to formulate the winding topology design as a classical optimization problem with

constraints and objectives. It will be seen that the necessary constraints do not require the slot-pole configuration to be conventional. Eventually, three objectives, depending on the harmonic content, are taken into account: the maximization of the fundamental, the minimization of the magnet losses and the minimization of the UMP.

In Chapter 3, the design procedure of a prototype machine which implements an unconventional FSCW is presented. Finally, the results of the tests on the prototype are presented to confirm the FSCW feasibility and its expected performance.

References

- [1] A.M. EL-Refaie. “Fractional-Slot Concentrated-Windings Synchronous Permanent Magnet Machines: Opportunities and Challenges”. In: *IEEE Transactions on Industrial Electronics* 57.1 (2010), pp. 107–121. ISSN: 0278-0046. DOI: 10.1109/TIE.2009.2030211. URL: <http://ieeexplore.ieee.org/document/5229186/>.
- [2] Alberto Tassarolo et al. “Design for Manufacturability of an Off-Shore Direct-Drive Wind Generator: An Insight Into Additional Loss Prediction and Mitigation”. In: *IEEE Transactions on Industry Applications* 53.5 (Sept. 2017), pp. 4831–4842. ISSN: 0093-9994. DOI: 10.1109/TIA.2017.2700285. URL: <http://ieeexplore.ieee.org/document/7917376/>.
- [3] Christopher M. Spargo et al. “Design and Validation of a Synchronous Reluctance Motor With Single Tooth Windings”. In: *IEEE Transactions on Energy Conversion* 30.2 (June 2015), pp. 795–805. ISSN: 0885-8969. DOI: 10.1109/TEC.2014.2384476. URL: <http://ieeexplore.ieee.org/lpdocs/epic03/wrapper.htm?arnumber=7006733>.
- [4] Emanuele Fornasiero et al. “Considerations on selecting fractional—slot windings”. In: *2010 IEEE Energy Conversion Congress and Exposition*. d. IEEE, Sept. 2010, pp. 1376–1383. ISBN: 978-1-4244-5286-6. DOI: 10.1109/ECCE.2010.5618269. URL: <https://ieeexplore.ieee.org/document/5618269/>.
- [5] Nicola Bianchi and Emanuele Fornasiero. “Impact of MMF Space Harmonic on Rotor Losses in Fractional-Slot Permanent-Magnet Machines”. In: *IEEE Transactions on Energy Conversion* 24.2 (June 2009), pp. 323–328. ISSN: 0885-8969. DOI: 10.1109/TEC.2008.2006557. URL: <http://ieeexplore.ieee.org/document/4611111>.

- [//ieeexplore.ieee.org/document/6022788/](http://ieeexplore.ieee.org/document/6022788/)<http://ieeexplore.ieee.org/document/4757261/>.
- [6] Alberto Tassarolo. “A survey of state-of-the-art methods to compute rotor eddy-current losses in synchronous permanent magnet machines”. In: *2017 IEEE Workshop on Electrical Machines Design, Control and Diagnosis (WEMDCD)*. IEEE, Apr. 2017, pp. 12–19. ISBN: 978-1-5090-5853-2. DOI: [10.1109/WEMDCD.2017.7947717](https://doi.org/10.1109/WEMDCD.2017.7947717). URL: <http://ieeexplore.ieee.org/document/7947717/>.
- [7] Fu Lin, Shuguang Zuo, and Xudong Wu. “Electromagnetic vibration and noise analysis of permanent magnet synchronous motor with different slot-pole combinations”. In: *IET Electric Power Applications* 10.9 (Nov. 2016), pp. 900–908. ISSN: 1751-8660. DOI: [10.1049/iet-epa.2016.0044](https://doi.org/10.1049/iet-epa.2016.0044). URL: <https://digital-library.theiet.org/content/journals/10.1049/iet-epa.2016.0044>.
- [8] Seun Guy Min and Bulent Sarlioglu. “Investigation of electromagnetic noise on pole and slot number combinations with possible fractional-slot concentrated windings”. In: *2017 IEEE Transportation Electrification Conference and Expo (ITEC)*. 1. IEEE, June 2017, pp. 241–246. ISBN: 978-1-5090-3953-1. DOI: [10.1109/ITEC.2017.7993278](https://doi.org/10.1109/ITEC.2017.7993278). URL: <http://ieeexplore.ieee.org/document/7993278/>.
- [9] Mostafa Valavi et al. “Influence of Pole and Slot Combinations on Magnetic Forces and Vibration in Low-Speed PM Wind Generators”. In: *IEEE Transactions on Magnetics* 50.5 (May 2014), pp. 1–11. ISSN: 0018-9464. DOI: [10.1109/TMAG.2013.2293124](https://doi.org/10.1109/TMAG.2013.2293124). URL: <http://ieeexplore.ieee.org/lpdocs/epic03/wrapper.htm?arnumber=6677574>.
- [10] Z.Q. Zhu and David Howe. “Influence of design parameters on cogging torque in permanent magnet machines”. In: *IEEE Transactions on Energy Conversion* 15.4 (2000), pp. 407–412. ISSN: 08858969. DOI: [10.1109/60.900501](https://doi.org/10.1109/60.900501). URL: <http://ieeexplore.ieee.org/document/900501/>.
- [11] Li Zhu et al. “Analytical Methods for Minimizing Cogging Torque in Permanent-Magnet Machines”. In: *IEEE Transactions on Magnetics* 45.4 (Apr. 2009), pp. 2023–2031. ISSN: 0018-9464. DOI: [10.1109/TMAG.2008.2011363](https://doi.org/10.1109/TMAG.2008.2011363). URL: <http://ieeexplore.ieee.org/document/4802358/>.
- [12] Luigi Alberti and Nicola Bianchi. “Theory and design of fractional-slot multilayer windings”. In: *2011 IEEE Energy Conversion Congress and*

- Exposition*. 1. IEEE, Sept. 2011, pp. 3112–3119. ISBN: 978-1-4577-0542-7. DOI: 10.1109/ECCE.2011.6064188. URL: <http://ieeexplore.ieee.org/document/6064188/>.
- [13] J.F. Gieras. *Electrical Machines: Fundamentals of Electromechanical Energy Conversion*. CRC Press, 2016. ISBN: 9781498708845. URL: <https://books.google.it/books?id=XR4NDgAAQBAJ>.

Chapter 1

FSCW and Extended-FSCW formalization

In this chapter the conventional and the unconventional design of a multi-layer FSCW topology is presented and mathematically formalised. The formalisation, applicable for multiphase windings, will be used to derive the harmonic content of the winding. Eventually, the harmonic content will be analytically examined to derive the mutual dependence among harmonics and to calculate the winding factor. Finally the harmonic contribution of a surface mounted permanent magnet (SPM) rotor is equally developed.

1.1 Topolgy description

In any kind of electrical rotating machine some fundamental parameters are defined by design, such as the number of phases (L), the number of pole pairs (p) and the number of slots (Z). The ratio

$$q = \frac{Z}{2p \cdot L} \quad (1.1)$$

expresses the slots per pole per phase. The most common machines are designed with distributed winding and with an integer q , which implies a number of slots equal to $Z = 2p \cdot Lq$ and each coil embraces several teeth.

In FSCW machines all coils are wound around a single tooth (concentrated winding). In particular, the number of layers describes the number of coil sides that can be found in a slot. It has been shown [1] that, in order to achieve a good winding factor, the ratio between the

number of poles and the number of teeth must be near unity. To obtain this, q must be fractional:

$$\frac{Z}{2p} \approx 1 \iff q \approx \frac{1}{L} \quad (1.2)$$

The coil arrangement around the stator can be defined by a simple algorithm [2], referred to as the star of slots. The star of slots can be used to design single or double layer windings, but a constraint must be met for the winding feasibility:

$$\frac{Z}{L \cdot \gcd(Z, p)} \in \mathbb{N} \quad (1.3)$$

where $\gcd(Z, p)$ represents the greatest common divisor between the arguments. The machines that meet this constraint will be referred to as conventional while the others will be referred to as unconventional.

In double layer FSCWs, a single coil of N_t turns is wound around each tooth. The notation “Extended” FSCW is referred to windings in which on each tooth the N_t turns can consist of more than one coil belonging to different phases. Of course, to design a winding with an arbitrary number of turns of different phases around each tooth requires to define a suitable mathematical model to represent the winding and optimize it, as explained in the next sections.

1.2 Stator contribution to air gap harmonic content

While developing formulas for the stator and rotor magnetomotive force production, a matrix notation will be defined, which allows for more compact symbolic expressions and makes the implementation through symbolic and numerical software both easier and more efficient and will allow to make some statements derived from linear algebra.

1.2.1 Basic definitions

It is worth noting that, for a three phase current, the phasors are displaced by $2\pi/3$ electrical radians and this approach can be generalized to any odd L number of phases adopting a $2\pi/L$ electrical displacement.

Clearly, if the opposite of phase X has to be applied to a coil, indeed the coil can be connected to phase X exchanging the connections, which makes an hypothetical -X phase redundant. When L is an even number, adopting a $2\pi/L$ electrical displacement would lead to a configuration in which half the phases are redundant.

To overcome this problem a different approach is necessary. Using a redundant number of phasors, numbered from zero to $2L-1$, with the $2L$ phasors equally spaced, the first L phasors ($l = 0, \dots, L-1$) correspond to the actual phases, the other L phasors ($l = L, \dots, 2L-1$) correspond to “dummy” phases, as better explained next.

Each phase current is represented by its phasor:

$$\bar{i}_l = i \cdot e^{j(-\frac{\pi}{L}l)} \quad \text{with } i \geq 0 \quad \forall l = 0, \dots, 2L-1 \quad (1.4)$$

As an example, in Fig. 1.1 a three phase scheme is shown in its classical representation (Fig. 1.1a) and through the dummy phase representation (Fig. 1.1b).

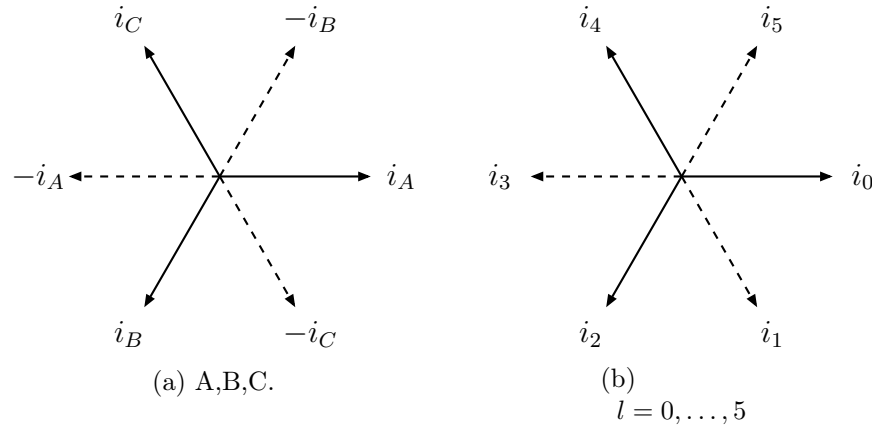


FIGURE 1.1: Phasor representation of three phase system: (a) classical and (b) dummy

The column vector $\bar{\mathbf{i}} \in \mathbb{C}^{[2L \times 1]}$ can be defined imposing $[\bar{\mathbf{i}}]_l = \bar{i}_l$. The currents in the time domain are given by

$$i_l(t) = \text{Re} \{ \bar{i}_l \cdot e^{j\omega t} \} = \text{Re} \{ [\bar{\mathbf{i}}]_l e^{j\omega t} \} \quad (1.5)$$

At this point the winding topology must be defined. The teeth are identified by $k = 0, \dots, Z-1$ and their axis is positioned at $\theta(k) = 2\pi \frac{k}{Z}$,

Table 1.1: (b) Highlighted in blue, example of winding matrix \mathbf{W} using dummy phases. (a) beside (highlighted in yellow) its correspondent representation using classic phases. The column index l is relative to the dummy phase, the row index k is relative to the tooth

(a) classic phases				(b) dummy phases							
$k \backslash$	A	B	C		$k \backslash l$	0 A^+	1 C^-	2 B^+	3 A^-	4 C^+	5 B^-
0	100	0	0		0	100	0	0	0	0	0
1	-100	0	0		1	0	0	0	100	0	0
2	0	0	-100		2	0	100	0	0	0	0
3	0	0	100		3	0	0	0	0	100	0
4	0	0	-100	\longleftrightarrow	4	0	100	0	0	0	0
5	0	-100	0		5	0	0	0	0	0	100
6	0	100	0		6	0	0	100	0	0	0
7	0	-100	0		7	0	0	0	0	0	100
8	-100	0	0		8	0	0	0	100	0	0

where θ is defined as the stator angular coordinate.

On tooth k , the positive number of turns of phase l is identified by $W_{k,l}$. The $[Z \times 2L]$ matrix \mathbf{W} , here called “winding matrix”, is defined so that the element in the k^{th} row and l^{th} column is $W_{k,l}$.

$$[\mathbf{W}]_{k,l} = W_{k,l} \quad (1.6)$$

As an example, a conventional winding for a three phase, 9 slots, 8 poles machine holding a hundred turns per tooth would be represented by the matrix in Tab. 1.1. In the following this machine will be referred to as the “conventional 9 – 8”

Using the notation defined by (1.5) and (1.6), the Magneto Motive Force (MMF) applied by each tooth, given by the sum of the contributions of the $2L$ phases, can be conveniently expressed in matrix form by the k^{th} element of the column vector resulting from the product $\mathbf{W} \cdot \bar{\mathbf{i}} e^{j\omega t}$

$$\text{MMF}_k(t) = \text{Re} \left\{ \sum_{l=0}^{2L-1} \{ W_{k,l} \cdot [\bar{\mathbf{i}}]_l e^{j\omega t} \} \right\} = \text{Re} \{ [\mathbf{W} \cdot \bar{\mathbf{i}}]_k e^{j\omega t} \} \quad (1.7)$$

1.2.2 Modelling space harmonics

This section is aimed at demonstrating that the harmonic content is determined by linear transformations involving the winding matrix (\mathbf{W}).

Defining matrix \mathbf{W} and the vector $\bar{\mathbf{i}}$, means to define the winding and the set of applied currents and therefore to define the magneto motive force (MMF). The shape of the MMF [3] that the stator generates in the gap at any position at any time is therefore completely defined.

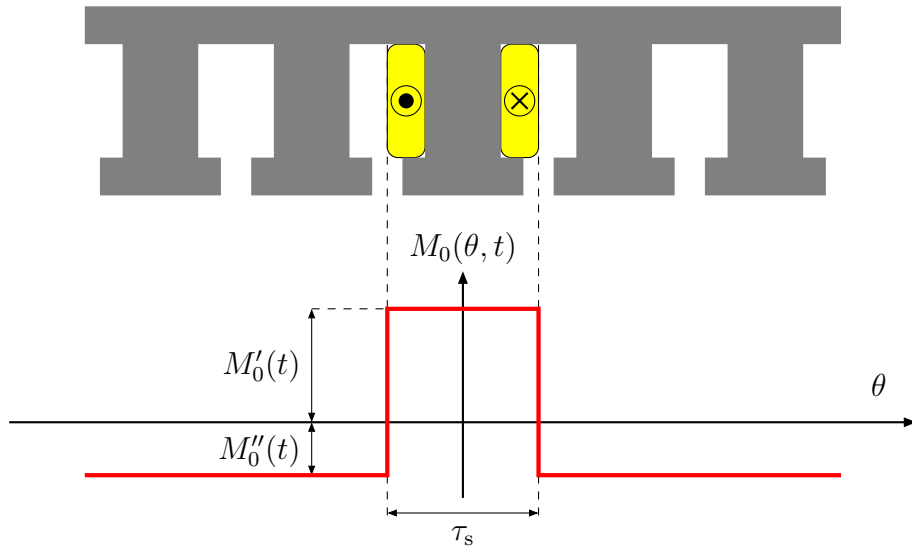


FIGURE 1.2: MMF along the gap angular coordinate θ at time t due to the sole tooth 0 contribution

The MMF due to the tooth $k = 0$, is represented in Fig. 1.2 and its value can be obtained as the real part of the complex function $\bar{M}_0(\theta, t)$ defined as follows:

$$\bar{M}_0(\theta, t) = \begin{cases} \bar{M}'_0(t) = \frac{Z-1}{Z}(\mathbf{W}\bar{\mathbf{i}}(t))_0 & \text{if } |\theta| \leq \frac{\tau_s}{2} \\ \bar{M}''_0(t) = -\frac{1}{Z}(\mathbf{W}\bar{\mathbf{i}}(t))_0 & \text{if } \frac{\tau_s}{2} \leq |\theta| \leq \pi \end{cases} \quad (1.8)$$

As the function is periodic over θ , it can be expanded in Fourier Series highlighting its spatial harmonic content (1.9),

$$\bar{M}_0(\theta, t) = \sum_{n=0}^{\infty} [a_n \cos(n\theta)] \cdot [\mathbf{W} \cdot \bar{\mathbf{i}}(t)]_0 \quad (1.9)$$

where the obtained Fourier coefficients are

$$a_n = \frac{2}{n\pi}(-1)^{n+1} \sin\left(\frac{n\pi \cdot (Z-1)}{Z}\right) \quad (1.10)$$

Observing (1.9) we can easily extend the definition to any tooth changing the index from 0 to k and shifting the angular position of k slot pitches: from θ to $\theta - 2\pi\frac{k}{Z}$.

$$\begin{aligned} \bar{M}_c^k(\theta, t) &= \sum_{n=0}^{\infty} \left\{ a_n \cos \left[n \left(\theta - \frac{2k\pi}{Z} \right) \right] \right\} \cdot [\mathbf{W} \cdot \bar{\mathbf{i}}(t)]_k \\ &= \sum_{n=0}^{\infty} \left\{ a_n \cos \left[n \left(\theta - \frac{2k\pi}{Z} \right) \right] \right\} \cdot e^{j\omega t} \cdot [\mathbf{W} \cdot \bar{\mathbf{i}}]_k \end{aligned} \quad (1.11)$$

The c subscript stands for column (the reason will be made clear after (1.14)).

At this point it is useful to separate the harmonic contributions of the teeth by defining $\bar{M}_{n,k}(\theta, t)$, which is an indexed scalar function whose value depends both on the arguments and on the indexes

$$\bar{M}_{n,k}(\theta, t) = \left\{ a_n \cos \left[n \left(\theta - \frac{2k\pi}{Z} \right) \right] \right\} \cdot e^{j\omega t} \cdot [\mathbf{W} \cdot \bar{\mathbf{i}}]_k \quad (1.12)$$

The total air gap MMF is obtained as $\text{Re}\{\bar{M}_s(\theta, t)\}$ (where the subscript S stands for stator), which can be calculated summing all the teeth contributions (1.13)

$$\begin{aligned} \bar{M}_s(\theta, t) &= \sum_{k=0}^{Z-1} \bar{M}_c^k(\theta, t) \\ &= \sum_{k=0}^{Z-1} \sum_{n=0}^{\infty} \bar{M}_{n,k}(\theta, t) \end{aligned} \quad (1.13)$$

From (1.13), the contribution to a specific space harmonic can be easily obtained considering only the corresponding term of the series instead of the whole series.

$$\bar{M}_r^n(\theta, t) = \sum_{k=0}^{Z-1} \bar{M}_{n,k}(\theta, t) \quad (1.14)$$

The “r” and “c” subscripts, standing for row and column, depend on the

fact that if $\bar{M}_{n,k}$ is considered as the generic element of a matrix, \bar{M}_r would be the sum along the n^{th} row (summing over k), while \bar{M}_c would be the sum along the k^{th} column (summing over n).

In Fig. 1.3 the resulting total MMF is represented in green along with its fundamental $\text{Re}\{\bar{M}_p(\theta, t)\}$ in red.

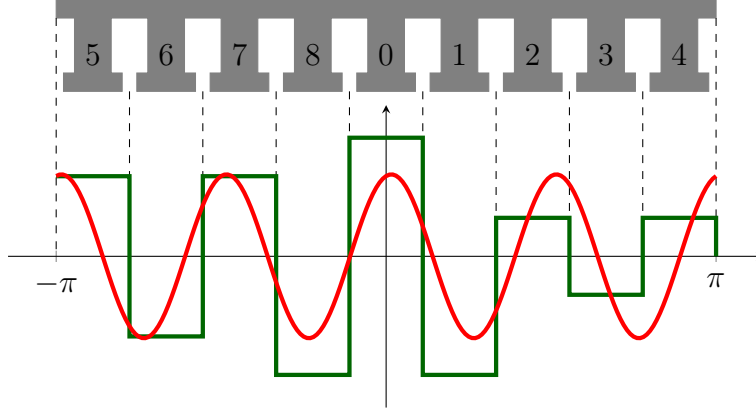


FIGURE 1.3: The MMF along the air gap angular coordinate θ for the conventional 9-8 configuration with $\omega t = 0.2$. In green the actual wave-shape, in red its fundamental ($n = p$).

In order to separate equi-rotating and counter-rotating harmonics we can decompose the cosine contained in (1.12) into two complex components and combine them with the time dependent exponential:

$$\begin{aligned} \cos\left(n\left(\theta - \frac{2k\pi}{Z}\right)\right) \cdot e^{j\omega t} &= \frac{1}{2} \left[e^{-j\left(n\left(\theta - \frac{2k\pi}{Z}\right)\right)} + e^{j\left(n\left(\theta - \frac{2k\pi}{Z}\right)\right)} \right] \cdot e^{j\omega t} \\ &= \frac{1}{2} \left[e^{j(\omega t - n\theta)} e^{jn\frac{2k\pi}{Z}} + e^{j(\omega t + n\theta)} e^{-jn\frac{2k\pi}{Z}} \right] \end{aligned} \quad (1.15)$$

A more compact notation can be given defining the indexed scalar function (1.16)

$$\bar{S}_{n,k}^{\oplus} = a_n \frac{1}{2} \left[e^{\pm j\left(n\frac{2k\pi}{Z}\right)} \right] \quad (1.16)$$

It is worth noting that with the present notation the symbol \ominus is related to the anti-clockwise rotating harmonics (positive mechanical

speed), while the symbol \oplus is related to clock-wise rotating harmonics (negative mechanical speed) and, because a_n is a real number, it is easy to see that $\bar{S}_{n,k}^\oplus$ is complex conjugate of $\bar{S}_{n,k}^\ominus$.

Equation (1.12), substituting (1.15) and (1.16), becomes

$$\begin{aligned}\bar{M}_{n,k}(\theta, t) &= \frac{a_n}{2} \left[e^{j(\omega t - n\theta)} e^{j\left(n\frac{2k\pi}{Z}\right)} + e^{j(\omega t + n\theta)} e^{-j\left(n\frac{2k\pi}{Z}\right)} \right] \cdot [\mathbf{W} \cdot \bar{\mathbf{i}}]_k \\ &= e^{j(\omega t - n\theta)} S_{n,k}^\ominus \cdot [\mathbf{W} \cdot \bar{\mathbf{i}}]_k + e^{j(\omega t + n\theta)} S_{n,k}^\oplus \cdot [\mathbf{W} \cdot \bar{\mathbf{i}}]_k\end{aligned}\quad (1.17)$$

Each spatial harmonic component is given by (1.18)

$$\bar{m}_n^\oplus = \sum_{k=0}^{Z-1} \bar{S}_{n,k}^\oplus \cdot [\mathbf{W} \cdot \bar{\mathbf{i}}]_k \quad (1.18)$$

The complex scalar \bar{m}_n^\oplus is a phasor, meaning that its module and phase represent amplitude and phase of the n^{th} counter-rotating (\oplus) or equi-rotating (\ominus) spatial harmonic, where “counter-” or “equi-” rotating is referred to the positive speed direction.

Equation (1.13), substituting (1.17) and then (1.18), becomes

$$\begin{aligned}\bar{M}_s(\theta, t) &= \sum_{k=0}^{Z-1} \sum_{n=0}^{\infty} \bar{M}_{n,k}(\theta) \\ &= \sum_{n=0}^{\infty} \left[e^{j(\omega t - n\theta)} \bar{m}_n^\ominus + e^{j(\omega t + n\theta)} \bar{m}_n^\oplus \right]\end{aligned}\quad (1.19)$$

Again, all the terms can be collected in vectors by defining the matrix $\bar{\mathbf{S}}^\oplus$ and the column harmonic vector $\bar{\mathbf{m}}^\oplus$

$$[\bar{\mathbf{S}}^\oplus]_{n,k} = \bar{S}_{n,k}^\oplus \quad (1.20)$$

$$[\bar{\mathbf{m}}^\oplus]_n = \bar{m}_n^\oplus \quad (1.21)$$

to obtain all the equi-rotating or the counter-rotating spatial harmonic components in a single operation.

$$\bar{\mathbf{m}}^\oplus = \bar{\mathbf{S}}^\oplus \mathbf{W} \cdot \bar{\mathbf{i}} \quad (1.22)$$

Algebraically, the selection of a specific harmonic n from a harmonic vector can be done defining \mathbf{s}_n as a selection row-vector having 1 in

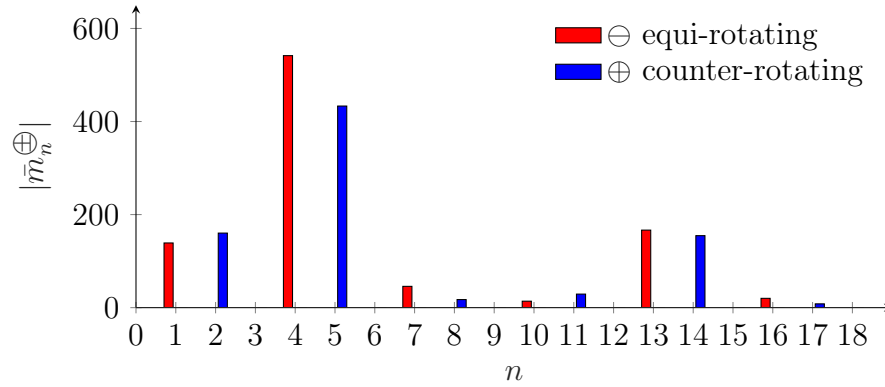


FIGURE 1.4: Amplitude of the harmonics produced by the star-of-slots winding in a conventional 9 – 8 configuration, in red the harmonics rotating anticlockwise like the fundamental, in blue the harmonics rotating clockwise.

position n and zero elsewhere, so that

$$\bar{m}_n^\oplus = \mathbf{s}_n \bar{\mathbf{m}}^\oplus \quad (1.23)$$

Finally, for the sake of completeness, to obtain the $\bar{M}(\theta, t)$ function using the matrix form it is possible to define the space-time row vector function as follows:

$$\left[\bar{\mathbf{e}}^\oplus(\theta, t) \right]_n = e^{j(\omega t \pm n\theta)} \quad (1.24)$$

and the following equation holds:

$$\bar{M}(\theta, t) = \bar{\mathbf{e}}^\oplus(\theta, t) \cdot \bar{\mathbf{m}}^\oplus + \bar{\mathbf{e}}^\ominus(\theta, t) \cdot \bar{\mathbf{m}}^\ominus \quad (1.25)$$

1.2.2.1 About the interpretation of the MMF components

Developing (1.25), the components in (1.26) can be found. In this section the meaning of the components will be summarized and in some cases an interpretation will be offered for its role.

$$\bar{M}_s(\theta, t) = \bar{\mathbf{e}}^\oplus(\theta, t) \cdot \overbrace{\bar{\mathbf{S}}^\oplus \mathbf{W} \cdot \bar{\mathbf{i}}}^{\bar{\mathbf{m}}^\oplus} + \bar{\mathbf{e}}^\ominus(\theta, t) \cdot \overbrace{\bar{\mathbf{S}}^\ominus \mathbf{W} \cdot \bar{\mathbf{i}}}^{\bar{\mathbf{m}}^\ominus} \quad (1.26)$$

$[\bar{\mathbf{i}}]$ — The column vector $\bar{\mathbf{i}}$ contains in each component a phasor defining the current of the corresponding phase, the dummy-phase notation being used (p. 7).

$[\mathbf{W}]$ — The winding matrix \mathbf{W} defines the number of turns for each phase and for each tooth. The row index corresponds to the tooth index while the column index corresponds to the dummy-phase index. With this notation the product $\mathbf{W} \cdot \bar{\mathbf{i}}$ gives a column vector in which the Z elements are the phasors corresponding to the total MMF imposed on each tooth.

$[\bar{\mathbf{S}}^\oplus]$ — The contribution to each MMF harmonic of each tooth depends both on the tooth position along the air gap and on the harmonic order. In matrix $\bar{\mathbf{S}}^\oplus$ the row index n represents the harmonic order and the column index k corresponds to the tooth index. The generic element of the matrix $(\bar{S}_{n,k}^\oplus)$ multiplied by the correspondent total tooth MMF $([\mathbf{W} \cdot \bar{\mathbf{i}}]_k)$ gives a phasor, which represents the contribution (in amplitude and phase) of tooth k to harmonic n . The product of the whole n^{th} row of $\bar{\mathbf{S}}^\oplus$ (i.e $\mathbf{s}_n \bar{\mathbf{S}}^\oplus$), by the whole column vector $\mathbf{W} \cdot \bar{\mathbf{i}}$, gives a phasor (\bar{m}_n^\oplus) which is the total contribution of all teeth to the n^{th} harmonic. Finally, the product of the whole $\bar{\mathbf{S}}^\oplus$ matrix by the $\mathbf{W} \cdot \bar{\mathbf{i}}$ vector gives a column vector $(\bar{\mathbf{m}}^\oplus)$ whose phasor elements represent the corresponding harmonic contributions of the winding.

$[\bar{\mathbf{e}}^\oplus(\theta, t)]$ — Finally, in order to calculate the MMF value in any point of the air gap and at any time, the harmonic phasors must be transformed into a sinusoid depending on space and time. The real part of each harmonic phasor corresponds to the starting point (i.e $t = 0$ and $\theta = 0$) of the corresponding sinusoidal wave. The value of the sinusoid, depending on the position and time (θ, t) , can be calculated multiplying the phasor by $[\bar{\mathbf{e}}^\oplus(\theta, t)]_n$. The complete shape of the air gap MMF is the sum of all the harmonic contributions, which can be calculated as the real part of the sum of the products of the row vectors $\bar{\mathbf{e}}^\oplus(\theta, t)$ and the respective harmonic vectors $\bar{\mathbf{m}}^\oplus$, which is (1.25).

1.2.3 Mutual dependence of space harmonics

At a first look, we can see that the harmonics produced by the stator are infinite. But clearly, a feasible machine design implies that the number of teeth, of turns per tooth and of phases is finite, so the number of possible configurations is finite and so the number of independent harmonics must be finite.

This section will be dedicated the demonstration of the following facts and their implications.

- The number of teeth (Z) determines the number of independent harmonics.
- The entire spectrum (on both rotation directions) can be derived from the first Z harmonics of any of the two directions.

The number of columns of $\bar{\mathbf{S}}^\oplus$ is Z , so the rank of the matrix can be no grater than Z , independently of the number n of harmonics (rows) that are considered. This implies that the maximum number of independent harmonics cannot be grater than Z . On the other hand, the first $Z - 1$ rows are linearly independent (which can be easily seen through a gaussian elimination), and this implies that the rank of $\bar{\mathbf{S}}^\oplus$ is $Z - 1$.

The two vectors $\bar{\mathbf{m}}^\ominus$ and $\bar{\mathbf{m}}^\oplus$ contain the entire MMF harmonic content information. To show how to derive the harmonics above the Z^{th} order, a generic element is now taken into account and expanded:

$$\begin{aligned} \bar{m}_n^\oplus &= \sum_{k=0}^{Z-1} \left[\overbrace{\frac{2}{n\pi}(-1)^{n+1} \sin\left(\frac{n\pi \cdot (Z-1)}{Z}\right) \frac{1}{2} e^{\mp j(n \frac{2k\pi}{Z})} [\mathbf{W} \cdot \bar{\mathbf{i}}]_k}^{\bar{S}_{n,k}^\oplus} \right] \\ &= \frac{1}{2} \frac{2}{n\pi}(-1)^{n+1} \sin\left(\frac{n\pi \cdot (Z-1)}{Z}\right) \sum_{k=0}^{Z-1} \left[e^{\mp j(n \frac{2k\pi}{Z})} [\mathbf{W} \cdot \bar{\mathbf{i}}]_k \right] \end{aligned} \quad (1.27)$$

Observing (1.27), the ratio between two harmonics rotating the same way \bar{m}_{n+Z}^\oplus and \bar{m}_n^\oplus can be found.

$$\frac{\bar{m}_{n+Z}^\oplus}{\bar{m}_n^\oplus} = \frac{a_{n+Z}}{a_n} \cdot \frac{\overbrace{\sum_{k=0}^{Z-1} e^{\mp j((n+Z) \frac{2k\pi}{Z})} [\mathbf{W} \cdot \bar{\mathbf{i}}]_k}^{=1}}{\sum_{k=0}^{Z-1} e^{\mp j(n \frac{2k\pi}{Z})} [\mathbf{W} \cdot \bar{\mathbf{i}}]_k} \quad (1.28)$$

The second factor of the product is equal to 1, so it gives no contribution to the ratio between \bar{m}_{n+Z}^\oplus and \bar{m}_n^\oplus . It can be seen that the

numerator of the second term is equal to the denominator considering the following

$$\begin{aligned}
 e^{\mp j(n+Z)\frac{2k\pi}{Z}} &= e^{\mp j(n\frac{2k\pi}{Z})} \cdot e^{\mp j(Z\frac{2k\pi}{Z})} \\
 &= e^{\mp j(n\frac{2k\pi}{Z})} \cdot e^{\mp j(2k\pi)} \\
 &= e^{\mp j(n\frac{2k\pi}{Z})}
 \end{aligned} \tag{1.29}$$

So the ratio is determined by the first factor:

$$\begin{aligned}
 \frac{a_{n+Z}}{a_n} &= \frac{\frac{2}{(n+Z)\pi}(-1)^{(n+Z)+1} \sin\left(\frac{(n+Z)\pi \cdot (Z-1)}{Z}\right)}{\frac{2}{n\pi}(-1)^{n+1} \sin\left(\frac{n\pi \cdot (Z-1)}{Z}\right)} \\
 &= \frac{n}{n+Z}(-1)^Z \frac{\sin\left(\frac{n\pi \cdot (Z-1)}{Z} + [\pi \cdot (Z-1)]\right)}{\sin\left(\frac{n\pi \cdot (Z-1)}{Z}\right)} \\
 &= \frac{n}{n+Z}(-1)^Z \frac{(-1)^{Z+1} \sin\left(\frac{n\pi \cdot (Z-1)}{Z}\right)}{\sin\left(\frac{n\pi \cdot (Z-1)}{Z}\right)} \\
 &= \frac{-n}{n+Z}
 \end{aligned} \tag{1.30}$$

By induction, the result can be extended stating that

$$\bar{m}_{n+hZ}^{\oplus} = \frac{n(-1)^h}{n+hZ} \cdot \bar{m}_n^{\oplus} \quad \text{where } h = 1, 2, \dots \tag{1.31}$$

In Fig. 1.5 the amplitudes of all the harmonics are shown, in red the ones rotating like the fundamental (i.e. $n = p = 4$), in blue the ones rotating the other way and in green the function reported in (1.32)

$$f(p, n) = \frac{p}{n} \cdot |\bar{m}_p^{\ominus}| \tag{1.32}$$

It can be observed that the function $f(p, n)$ intercepts the fundamental harmonic $n = p = 4$ and all the harmonics $n = p + hZ = 13, 22, 31, \dots$

A similar rule holds for opposite rotating harmonics respectively of order n' and n if $n' + n = Z$

$$\frac{\bar{m}_{n'}^{\oplus}}{\bar{m}_n^{\ominus}} = \frac{a_{n'}}{a_n} \cdot \overbrace{\frac{\sum_{k=0}^{Z-1} e^{-j(n'\frac{2k\pi}{Z})} [\mathbf{W} \cdot \bar{\mathbf{i}}]_k}{\sum_{k=0}^{Z-1} e^{+j(n\frac{2k\pi}{Z})} [\mathbf{W} \cdot \bar{\mathbf{i}}]_k}}^{=1} \tag{1.33}$$

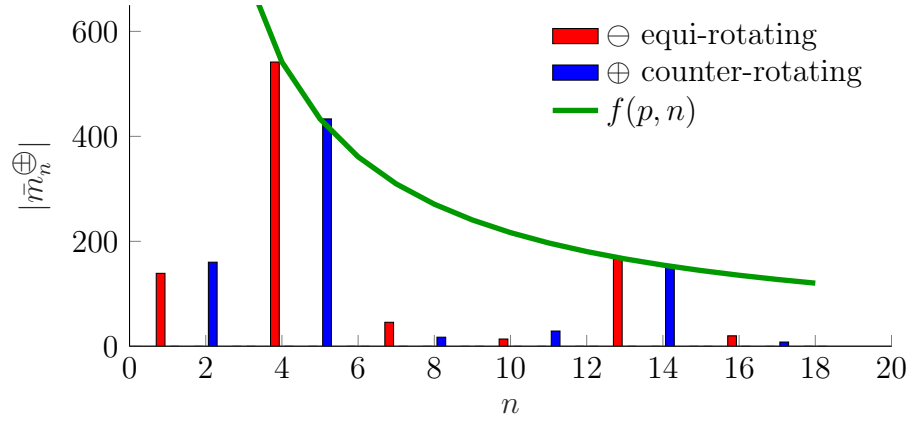


FIGURE 1.5: Amplitudes of the harmonics for a 9 teeth, 8 pole conventional configuration, in red the harmonics rotating anticlockwise as the fundamental, in blue the harmonics rotating clockwise, in green the function $f(p, n)$

considering that

$$\begin{aligned}
 e^{-j(n' \frac{2k\pi}{Z})} &= e^{-j(-(n-Z) \frac{2k\pi}{Z})} \\
 &= e^{+j((n-Z) \frac{2k\pi}{Z})} \\
 &= e^{+j(n \frac{2k\pi}{Z})} \cdot e^{-jZ \frac{2k\pi}{Z}} \\
 &= e^{+j(n \frac{2k\pi}{Z})}
 \end{aligned} \tag{1.34}$$

$$\begin{aligned}
\frac{\bar{m}_{n'}^{\oplus}}{\bar{m}_n^{\ominus}} &= \frac{a_{n'}}{a_n} = \frac{a_{Z-n}}{a_n} \\
&= \frac{\frac{2}{(Z-n)\pi}(-1)^{(Z-n)+1} \sin\left(\frac{(Z-n)\pi \cdot (Z-1)}{Z}\right)}{\frac{2}{n\pi}(-1)^{n+1} \sin\left(\frac{n\pi \cdot (Z-1)}{Z}\right)} \\
&= \frac{n}{Z-n}(-1)^Z \frac{\sin\left\{\frac{-n\pi \cdot (Z-1)}{Z} + [\pi \cdot (Z-1)]\right\}}{\sin\left(\frac{n\pi \cdot (Z-1)}{Z}\right)} \\
&= \frac{n}{Z-n}(-1)^Z \frac{(-1)^{(Z-1)} \left[-\sin\left(\frac{n\pi \cdot (Z-1)}{Z}\right)\right]}{\sin\left(\frac{n\pi \cdot (Z-1)}{Z}\right)} \\
&= \frac{n}{Z-n}(-1)^Z \frac{(-1)^{(Z-1)}(-1) \sin\left(\frac{n\pi \cdot (Z-1)}{Z}\right)}{\sin\left(\frac{n\pi \cdot (Z-1)}{Z}\right)} \\
&= \frac{n}{Z-n} \quad n \neq Z
\end{aligned} \tag{1.35}$$

For this reason, as can be seen in Fig. 1.5, the same function intercepting the equi-rotating harmonics $p, p+Z, p+2Z, \dots$ intercepts also the counter-rotating harmonic $Z-p=5$ and all the counter-rotating harmonics obtained summing hZ , which are $2Z-p=14, 3Z-p=23, \dots$

It should be noted the the dependence of the MMF harmonics is due only to the number of teeth in the stator, the winding topology is not involved. This means that once the number of teeth is chosen, all harmonics are divided in Z “families”, in each family the module and the phase are linked to the ones of the other members. Every harmonic family H_k can be identified by the following rule

$$\begin{aligned}
H_k &= \left\{ \{n^{\ominus} : n^{\ominus} = k + hZ\} \cup \{n^{\oplus} : n^{\oplus} = hZ - k\} \middle| h \in \mathbb{N} \right\} \\
&\quad k = 0, \dots, Z-1 \tag{1.36}
\end{aligned}$$

where the elements included in the $\{n^{\ominus} = k + hZ\}$ set are the harmonic order of positive rotating (anticlockwise or \ominus) harmonics, while the elements included in the $\{n^{\oplus} = hZ - k\}$ set are the harmonic order of negative rotating (clockwise or \oplus) harmonics. In this way every family is named after the first equi-rotating harmonic contained in its set. It

should be noted that all harmonic amplitudes relative to the family H_0 (m_{hZ}^\oplus) are equal to 0.

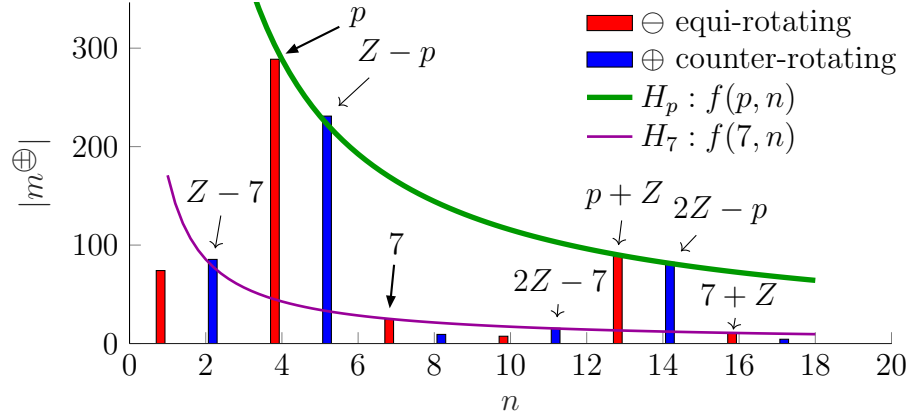


FIGURE 1.6: Amplitudes of the harmonics for a 9 – 8 conventional configuration. The function $f(p, n)$ (in green) highlights the members of the family H_p . The function $f(7, n)$ (in purple) highlights the members of the family H_7

In Fig. 1.6 the linkage among the amplitudes of the members of two families is highlighted. The family H_p includes the indexes p^\ominus , $(Z - p)^\oplus$, $(p + Z)^\ominus$, $(2Z - p)^\oplus$, ... Similarly, the family H_7 includes the members 7^\ominus , $(Z - 7)^\oplus$, $(7 + Z)^\ominus$, $(2Z - 7)^\oplus$, ...

It can be easily seen that the relation between harmonics holds for (or comes from) the rows of the $\bar{\mathbf{S}}^\oplus$ matrices:

$$\begin{aligned} \bar{S}_{(n+hZ),k}^\oplus &= \frac{n(-1)^h}{hZ+n} \cdot \bar{S}_{n,k}^\oplus \quad \text{with } h = 1, 2, \dots \\ \bar{S}_{(Z-n),k}^\oplus &= \frac{n}{Z-n} \cdot \bar{S}_{n,k}^\ominus \quad \text{with } n < Z \end{aligned} \quad (1.37)$$

This fact is particularly interesting because it makes clear that the dependence between harmonics depends only on the number of teeth in the stator. The number of poles, of phases and the winding topology are not involved.

In their first formulation, $\bar{\mathbf{S}}^\ominus$ and $\bar{\mathbf{S}}^\oplus$ have n rows, where n is not limited. Because of the harmonic dependence, it is sufficient to define only the first Z rows of one of the two (making them square $Z \times Z$ matrices). For example $\bar{\mathbf{S}}^\ominus$ can be chosen, being needed for the fundamental, to have a full view of the winding harmonic content. The first Z opposite rotating harmonics can be obtained by (1.37), the harmonics

over the Z^{th} order of both rotation ways can be obtained applying the appropriate coefficient defined in (1.31).

Furthermore, while observing (1.16) it can be seen that $\bar{\mathbf{S}}^{\ominus}$ is simply the complex conjugate of $\bar{\mathbf{S}}^{\oplus}$, observing (1.22), $\bar{\mathbf{m}}^{\ominus}$ does not inherit this property (it is not the complex conjugate of $\bar{\mathbf{m}}_n^{\oplus}$) because of the phase contribution given by $\mathbf{W} \cdot \bar{\mathbf{i}}$.

1.2.4 Winding factor computation

In general, the winding factor κ_w , ranging between 0 and 1, indicates the effectiveness of a winding to produce or link the fundamental space harmonic. Because the winding factor is also commonly calculated for other space harmonics, depending both on the harmonic order and the rotation direction, the notation will be κ_{wn}^{\ominus} or κ_{wn}^{\oplus} respectively for the n^{th} order anticlockwise or clockwise rotation.

In this section the developed notation will be firstly used to calculate the winding factor directly from the harmonic amplitudes and some winding data, secondly the chord factor is calculated and finally the distribution factor is derived.

For any winding, the n^{th} harmonic winding factor (κ_{wn}^{\oplus}) can be defined as the ratio between the space harmonic peak value produced by the actual winding ($|\bar{m}_n^{\oplus}|$) and the space harmonic peak value (\hat{m}_n) produced by a hypothetical winding, consisting of a single concentrated coil with a span equal to the n^{th} harmonic pole pitch and a number of turns equal to the sum of all the series connected turns of all phases as the actual winding [4].

$$\kappa_{wn}^{\oplus} = \frac{|\bar{m}_n^{\oplus}|}{\hat{m}_n} \quad (1.38)$$

The peak value of the harmonic of the actual winding $|\bar{m}_n^{\oplus}|$ can be calculated by (1.23).

$$|\bar{m}_n^{\oplus}| = s_n \bar{\mathbf{S}}^{\oplus} \mathbf{W} \cdot \bar{\mathbf{i}}$$

and the peak value of the hypothetical winding, is calculated as follows [5]:

$$\hat{m}_n = \frac{N_{\text{tot}} i_l}{n\pi} \quad (1.39)$$

where N_{tot} is the total number of turns of the machine (the sum of all the \mathbf{W} elements) and i_l is the phase current peak value.

The winding factor can be calculated as the product of the chord factor κ_c (also called pitch factor) and the distribution factor κ_d , as in (1.40). The first takes into account the effect of the difference between the pole pitch and the coil pitch, the second takes into account the positioning of the coils along the air gap.

$$\kappa_{wn}^{\oplus} = \kappa_{cn}^{\oplus} \kappa_{dn}^{\oplus} \quad (1.40)$$

The chord factor is purely geometric. As all coils have the same pitch, it can be easily calculated with the traditional formula [6]

$$\kappa_{cn}^{\oplus} = \sin \left(\frac{\tau_{\text{coil}} \pi}{\tau_p} \right) = \kappa_{cn} \quad (1.41)$$

where τ_{coil} represents the coil pitch. As can be seen in (1.41), the harmonic direction has no effect on the chord factor so the \oplus notation is unnecessary. Considering that in FSCW windings the coil pitch τ_{coil} coincides with the slot pitch and that the pole pitch (τ_p) of the n^{th} harmonic is half period of the space harmonic,

$$\tau_{\text{coil}} = \tau_s = \frac{2\pi}{Z} \quad \tau_n = \frac{2\pi}{2n} \quad (1.42)$$

the chord factor is obtained substituting (1.42) in (1.41)

$$\kappa_{cn} = \sin \left(\frac{n}{Z} \pi \right) \quad (1.43)$$

The distribution factor can be calculated simply as the ratio of the winding factor and the chord factor.

$$\kappa_{dn}^{\oplus} = \frac{\kappa_{wn}^{\oplus}}{\kappa_{cn}} \quad (1.44)$$

1.3 SPM rotor contribution to air gap harmonic content

The rotor MMF has a fixed shape due to the geometry of the SPMs and of the air gap, but its position will depend on time, mechanical speed and on its initial position.

The following references are fixed:

- the mechanical speed is considered proportional to the frequency so that the machine is working synchronously (positive rotating anti-clockwise);
- the poles are numbered from 1 to $2p$ anti-clockwise;
- odd numbered poles are “North”, meaning the flux density (B) is oriented from the rotor to the stator; consequently even numbered poles are “South”, with opposite B direction;
- the angular position of the first pole axis is taken as a reference for the rotor angular position.

Based on the cited references, the rotor angular position will be referred to as θ_R , the MMF will be initially calculated as $M_R(\theta_R)$, (relative to rotor angular reference) and eventually as a function of time (t) and stator referenced angle (θ)

For the rotor, the MMF contribution will be calculated considering radially magnetized magnets with constant height (h_{mag}), the magnet angular span is τ_{mag} , the pole pitch is referred to as τ_p and k_{mag} is the magnet span to pole pitch ratio. The waveform of the MMF can then be represented by a 3-level square wave (Fig. 1.7):

In order to define the M_R function, a normalized 3-level rectangular periodic function (rect_N) will now be defined in the $]-\pi, \pi]$ interval coinciding with its period (1.45), and represented in Fig. 1.8.

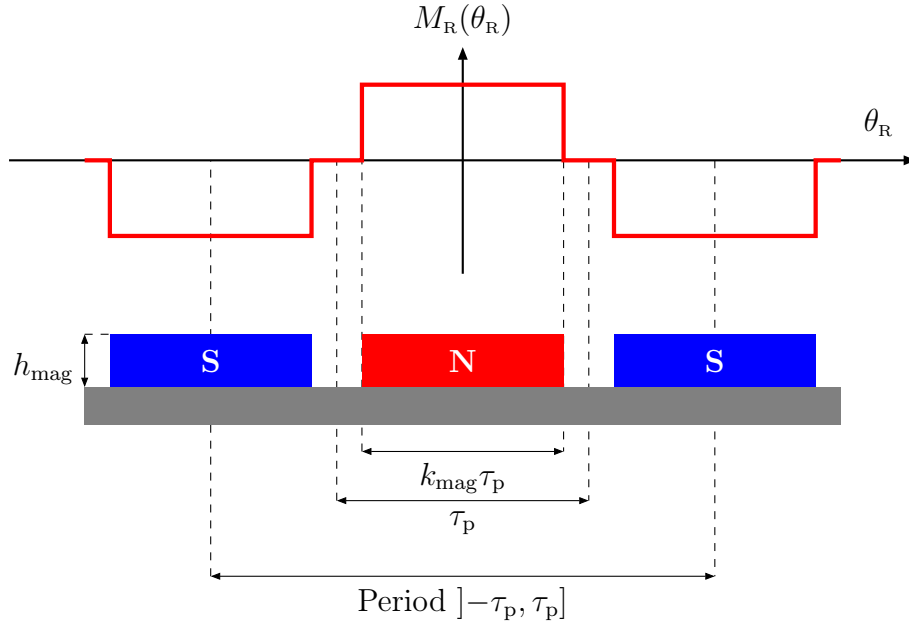


FIGURE 1.7: MMF due to the surface magnets, where θ is rotor referenced angular position. τ_p pole pitch, k_{mag} magnet width to pole pitch ratio and h_{mag} magnet height.

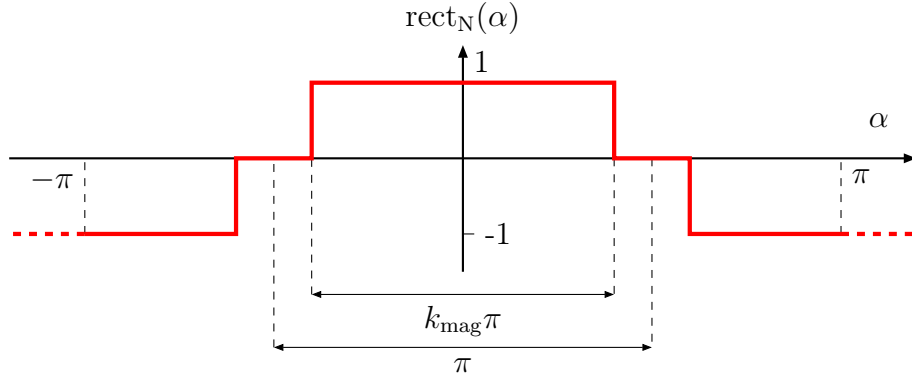
$$\text{rect}_N(\alpha)|_{]-\pi, \pi]} = \begin{cases} 1 & \text{if } |\alpha| \leq \frac{k_{\text{mag}}\pi}{2} \\ 0 & \text{if } \frac{k_{\text{mag}}\pi}{2} < |\alpha| \leq \pi - \frac{k_{\text{mag}}\pi}{2} \\ -1 & \text{if } \pi - \frac{k_{\text{mag}}\pi}{2} < |\alpha| < \pi \text{ or } \alpha = \pi \end{cases} \quad (1.45)$$

As rect_N is a periodic even function, it can be fully represented by its cosine Fourier series development. In (1.46) the n^{th} coefficient is calculated.

$$r_n = \frac{2}{n\pi} \sin\left(\frac{k_{\text{mag}} n\pi}{2}\right) \cdot (1 - (-1)^n) \quad (1.46)$$

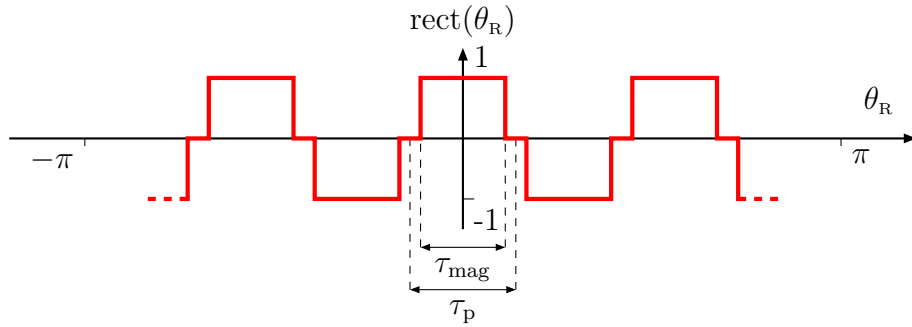
It can be seen that all coefficients of even order are zero.

As can be seen from Fig. 1.8, (1.45) represents a 2 pole machine but, generally, a function representing $2p$ poles on the $]-\pi, \pi]$ geometric domain will be needed. Such function can be easily obtained by its Fourier series (1.47), that is represented in Fig. 1.9, where the magnet width τ_{mag} is defined as $\tau_{\text{mag}} = k_{\text{mag}}\tau_p$ and the rotor referenced angular

FIGURE 1.8: Normalized $\text{rect}_N(\alpha)$ on its 2π period

coordinate is defined as θ_R .

$$\text{rect}(\theta_R) = \sum_{n=1}^{\infty} r_n \cos(pn\theta_R) \quad (1.47)$$

FIGURE 1.9: $\text{rect}(\theta_R)$ representation with arbitrary number of p pole pairs, where τ_p is the pole pitch and τ_{mag} is the angular magnet width

The function $\text{rect}(\theta_R)$, multiplied by the maximum value of the MMF, defines $M_R(\theta_R)$ in (1.48) by .

$$M_R(\theta_R) = M_{R,\text{max}} \cdot \text{rect}(\theta_R) \quad (1.48)$$

Finally, the MMF waveform has been expressed in the rotor-referenced coordinate θ_R , (1.49) must be used to pass to the absolute θ reference

$$\theta_R = \theta - \theta_0 - \frac{\omega t}{p} \quad (1.49)$$

The complete expression is given in (1.50) depending explicitly on time (t) and on pole pairs (p), on the initial rotor position (θ_0) and on the electrical pulsation (ω).

$$\begin{aligned}
 M_R(\theta, t) &= M_{R,\max} \cdot \text{rect} \left(\theta - \theta_0 - \frac{\omega t}{p} \right) \\
 &= M_{R,\max} \cdot \sum_{n=1}^{\infty} r_n \cos(pn(\theta - \theta_0 - \frac{\omega t}{p})) \\
 &= \text{Re} \left[M_{R,\max} \cdot \sum_{n=1}^{\infty} r_n e^{jn(p(\theta - \theta_0) - \omega t)} \right]
 \end{aligned} \tag{1.50}$$

Defining the stator contribution as in (1.51), the full MMF contribution content in the air gap is given by (1.52)

$$M_s(\theta, t) = \text{Re} [\bar{M}_s(\theta, t)] \tag{1.51}$$

$$\begin{aligned}
 M(\theta, t) &= \\
 &= M_R(\theta, t) + M_s(\theta, t) \\
 &= \text{Re} \left\{ M_{R,\max} \cdot \sum_{n=1}^{\infty} r_n e^{jn(p(\theta - \theta_0) - \omega t)} + \sum_{n=0}^{\infty} e^{j(\omega t + n\theta)} \bar{m}_n^{\ominus} + e^{j(\omega t - n\theta)} \bar{m}_n^{\oplus} \right\} \\
 &= \text{Re} \left\{ \sum_{n=1}^{\infty} M_{R,\max} \cdot e^{jn(p(\theta - \theta_0) - \omega t)} r_n + e^{j(\omega t + n\theta)} \bar{m}_n^{\ominus} + e^{j(\omega t - n\theta)} \bar{m}_n^{\oplus} \right\}
 \end{aligned} \tag{1.52}$$

References

- [1] Seun Guy Min and Bulent Sarlioglu. “Investigation of electromagnetic noise on pole and slot number combinations with possible fractional-slot concentrated windings”. In: *2017 IEEE Transportation Electrification Conference and Expo (ITEC)*. 1. IEEE, June 2017, pp. 241–246. ISBN: 978-1-5090-3953-1. DOI: [10.1109/ITEC.2017.7993278](https://doi.org/10.1109/ITEC.2017.7993278). URL: <http://ieeexplore.ieee.org/document/7993278/>.
- [2] Nicola Bianchi and M. Dai Pre. “Use of the star of slots in designing fractional-slot single-layer synchronous motors”. In: *IEE Proceedings - Electric Power Applications* 153.3 (2006), p. 459. ISSN: 13502352. DOI:

- 10.1049/ip-epa:20050284. URL: https://digital-library.theiet.org/content/journals/10.1049/ip-epa%7B%5C_%7D20050284.
- [3] Fabio Luise et al. “Regenerative Testing of a Concentrated-Winding Permanent-Magnet Synchronous Machine for Offshore Wind Generation—Part I: Test Concept and Analysis”. In: *IEEE Transactions on Industry Applications* 48.6 (Nov. 2012), pp. 1779–1790. ISSN: 0093-9994. DOI: 10.1109/TIA.2012.2221072. URL: <http://ieeexplore.ieee.org/document/6317167/>.
- [4] R.F. Burbidge. “A rapid method of analysing the m.m.f. wave of a single or polyphase winding”. In: *Proceedings of the IEE Part C: Monographs* 105.7 (1958), p. 307. ISSN: 03698904. DOI: 10.1049/pi-c.1958.0037. URL: <https://digital-library.theiet.org/content/journals/10.1049/pi-c.1958.0037>.
- [5] Alberto Tassarolo et al. “Investigation into Multi-Layer Fractional-Slot Concentrated Windings with Unconventional Slot-Pole Combinations”. In: *IEEE Transactions on Energy Conversion* 8969.c (2019), pp. 1–1. ISSN: 0885-8969. DOI: 10.1109/TEC.2019.2929950. URL: <https://ieeexplore.ieee.org/document/8767954/>.
- [6] Valeria Hrabovcova Juha Pyrhonen Tapani Jokinen. *Design of Rotating Electrical Machines*. 2nd ed. Wiley, Dec. 2013. ISBN: 978-1-118-58157-5.

Chapter 2

FSCW air gap harmonic content optimization

In general, an optimization problem implies the definition of an objective function that combines all variables to obtain a single real number, so that the optimum can be defined as the maximum or minimum of the objective function. In most cases, some kind of constraints are applied to variables.

In our case, some quantities of interest depend on the harmonic content of the flux density in the air gap, like the torque, eddy current losses or the UMP.

As an example, the average torque depends on the fundamental space harmonic amplitude, eddy current losses depend on a quadratic function of all harmonics, UMP depends on the products of neighbour harmonics.

Normally optimizing algorithms act on a set of variables which are organized in a vector. By this approach constraints and objectives can be easily defined both for linear and quadratic cases through well known algebraic operations. It is important to notice that efficiency and efficacy of optimization algorithms depend on the number of variables and the problem type complexity, which depends on the objective function and on the constraints definition. For instance a problem defined by a linear objective and over linear constraints can be solved very quickly and exactly by specific algorithms. As non-linearities are introduced, complexity grows and finally algorithms have to be used that cannot take advantage of any property of the objective function and which can only find an approximate local solution.

The compact formalization defined in [chapter 1](#) is very efficient to

obtain the harmonic vectors $\bar{\mathbf{m}}^\pm$, but optimization algorithms are normally defined to act on vector variables, therefore the winding matrix \mathbf{W} elements must be reorganised into a vector in order to be treatable by known specifically designed algorithms. A reasonable way to reorganise the winding matrix is to define a winding vector \mathbf{w} , through the following vectorizing operation

$$[\mathbf{w}]_{2Lk+l} = [\mathbf{W}]_{k,l} \quad \forall k, l \quad (2.1)$$

When the winding vector is defined as in (2.1), the following identity can be verified

$$\mathbf{W} \mathbf{A} \equiv [\mathbb{I}_Z \otimes \mathbf{A}^T] \mathbf{w} \quad (2.2)$$

where \mathbf{A} represents any matrix (having $2L$ rows), \mathbb{I}_Z represents the identity matrix of order Z and \otimes represents the Kronecker product, as an example the product in (2.2) is developed in (2.3).

$$\mathbb{I}_Z \otimes \mathbf{A}^T = \begin{bmatrix} \mathbf{A}^T & \mathbf{0} & \dots & \mathbf{0} \\ \mathbf{0} & \mathbf{A}^T & \ddots & \vdots \\ \vdots & \ddots & \ddots & \mathbf{0} \\ \mathbf{0} & \dots & \mathbf{0} & \mathbf{A}^T \end{bmatrix} \quad (2.3)$$

where $\mathbf{0}$ indicates a zero valued matrix of the same size of \mathbf{A}^T .

The effect of a winding on the generic n^{th} harmonic (\bar{m}_n^\pm) can be obtained taking the n^{th} element of its harmonics vector ($\bar{\mathbf{m}}^\pm$) using the selection vector as defined in (1.23).

$$\begin{aligned} \bar{m}_n^\oplus &= \mathbf{s}_n \bar{\mathbf{m}}^\oplus \\ &= \mathbf{s}_n \bar{\mathbf{S}}^\oplus \mathbf{W} \bar{\mathbf{i}} \\ &= \mathbf{s}_n \bar{\mathbf{S}}^\oplus [\mathbb{I}_Z \otimes \bar{\mathbf{i}}^T] \mathbf{w} \end{aligned} \quad (2.4)$$

so, by defining the complex line vector $\bar{\mathbf{v}}_n^\oplus \in \mathbb{C}^{1 \times 2LZ}$

$$\bar{\mathbf{v}}_n^\oplus = \mathbf{s}_n \bar{\mathbf{S}}^\oplus [\mathbb{I}_Z \otimes \bar{\mathbf{i}}^T] \quad (2.5)$$

the following can be written

$$\bar{m}_n^\oplus = \bar{\mathbf{v}}_n^\oplus \mathbf{w} \quad (2.6)$$

Equations (2.2) – (2.6) will be used to rewrite some equations defined for the winding matrix in the winding vector form.

2.1 Constraints

In this section it will be shown how the constraints used for all optimization problems are defined. It will also be shown that constraints are linear, divided between (a) equality constraints and (b) inequality constraints, expressed in the following forms.

$$a) \mathbf{Ax} = \mathbf{b} \quad b) \mathbf{Ax} \leq \mathbf{b} \quad (2.7)$$

In the first constraint, all the elements of \mathbf{W} must be positive to comply with the convention described in Section 1.2.1

$$W_{k,l} \geq 0 \quad \forall k, l \quad (2.8)$$

Defining $\mathbf{0}_n$ as a column vector of n elements equal to zero and \mathbb{I}_{2LZ} the identity matrix of rank $2LZ$,

$$\mathbf{A_0 w} \leq \mathbf{0}_{2LZ} \quad (2.9)$$

where $\mathbf{A_0} = -\mathbb{I}_{2LZ}$.

In the second constraint, the number of turns that can be wound on a tooth is limited, so, if N_t is the maximum number of turns per tooth and $\mathbf{1}_n$ as a column vector of n elements equal to one, the following constraint is defined:

$$\sum_{l=0}^{2L-1} W_{k,l} \leq N_t \quad \forall k \quad (2.10)$$

or, in matrix form

$$\mathbf{W} \mathbf{1}_{2L} \leq N_t \cdot \mathbf{1}_Z \quad (2.11)$$

Equation (2.11) represents a linear constraint, that using (2.2) can be rewritten in the matrix form (as defined in (2.7)) for the winding vector:

$$\mathbf{A_T w} \leq N_t \cdot \mathbf{1}_Z \quad \text{with} \quad \mathbf{A_T} = \mathbb{I}_Z \otimes \mathbf{1}_{2L}^T \quad (2.12)$$

In the third constraint, the winding is required to be symmetric, which implies that all phases give the same contribution to the MMF fundamental harmonic (\bar{m}_p^\ominus).

The contribution of a single phase to the fundamental MMF harmonic could be easily obtained by (1.22), using a winding matrix of a single phase derived from \mathbf{W} . This can be done defining \mathbf{K}_l as a $2L \times 2L$ symmetric matrix having 1 in positions (l, l) and $(l + L, l + L)$ and zero elsewhere with the matrix indexes starting from 0. In this case $l = 0, \dots, L - 1$ because the same matrix takes into account the contribution both of phase l and its opposite, i.e. the dummy phase $l + L$. In (2.13) \mathbf{K}_0 is exemplified.

$$\mathbf{K}_0 = \begin{bmatrix} 1 & 0 & & \dots & & 0 \\ 0 & 0 & & & & \\ & & \ddots & & & \\ & & & 0 & & \vdots \\ \vdots & & & & 1 & \\ & & & & & 0 \\ & & & & & \ddots & 0 \\ 0 & & & \dots & & 0 & 0 \end{bmatrix} \quad (2.13)$$

The phase winding matrix and the corresponding phase winding vector are obtained as follows.

$$\mathbf{W}_l = \mathbf{W} \mathbf{K}_l \quad \mathbf{w}_l = (\mathbb{I}_Z \otimes \mathbf{K}_l) \mathbf{w} \quad (2.14)$$

the resulting $\mathbf{W}_l | \mathbf{w}_l$ is a winding matrix|vector with the same dimensions of $\mathbf{W} | \mathbf{w}$ having unmodified elements in the positions relative to phases l and $l + L$ and zeros elsewhere. Clearly, the complete winding matrix|vector can be obtained as a sum of all phase winding matrices|vectors

as can be seen in (2.15)

$$\begin{aligned} \sum_{l=0}^{L-1} \mathbf{w}_l &= \sum_{l=0}^{L-1} [\mathbf{W} \mathbf{K}_l] = \mathbf{W} \sum_{l=0}^{L-1} \mathbf{K}_l = \mathbf{W} \mathbb{I}_{2L} = \mathbf{W} \\ \sum_{l=0}^{L-1} \mathbf{w}_l &= \sum_{l=0}^{L-1} (\mathbb{I}_Z \otimes \mathbf{K}_l) \mathbf{w} = \left(\mathbb{I}_Z \otimes \sum_{l=0}^{L-1} \mathbf{K}_l \right) \mathbf{w} = (\mathbb{I}_Z \otimes \mathbb{I}_{2L}) \mathbf{w} = (\mathbb{I}_{2LZ}) \mathbf{w} = \mathbf{w} \end{aligned} \quad (2.15)$$

The contribution of each phase l to the fundamental harmonic is calculated applying (2.6) to the phase winding vector.

$$\bar{m}_{lp}^\ominus = \bar{\mathbf{v}}_p^\ominus \mathbf{w}_l \quad (2.16)$$

Imposing that all phases must produce the same fundamental harmonic means to impose the following $L - 1$ equations

$$\begin{aligned} \bar{m}_{lp}^\ominus &= \bar{m}_{l+1p}^\ominus \\ \bar{\mathbf{v}}_p^\ominus \mathbf{w}_l &= \bar{\mathbf{v}}_p^\ominus \mathbf{w}_{l+1} \\ \bar{\mathbf{v}}_p^\ominus (\mathbb{I}_Z \otimes \mathbf{K}_l) \mathbf{w} &= \bar{\mathbf{v}}_p^\ominus (\mathbb{I}_Z \otimes \mathbf{K}_{l+1}) \mathbf{w} \end{aligned} \quad (2.17)$$

$$[\bar{\mathbf{v}}_p^\ominus \mathbb{I}_Z \otimes (\mathbf{K}_l - \mathbf{K}_{l+1})] \mathbf{w} = 0 \quad l = 0, \dots, L - 2 \quad (2.18)$$

Equation (2.18) guarantees the symmetry of the phase windings. Following the defined constraint notation, (2.18) can be expressed as follows

$$\begin{bmatrix} \bar{\mathbf{v}}_p^\ominus [\mathbb{I}_Z \otimes (\mathbf{K}_0 - \mathbf{K}_1)] \\ \bar{\mathbf{v}}_p^\ominus [\mathbb{I}_Z \otimes (\mathbf{K}_1 - \mathbf{K}_2)] \\ \vdots \\ \bar{\mathbf{v}}_p^\ominus [\mathbb{I}_Z \otimes (\mathbf{K}_{L-2} - \mathbf{K}_{L-1})] \end{bmatrix} \mathbf{w} =: \bar{\mathbf{A}}_{\mathbf{S}} \mathbf{w} = 0 \quad (2.19)$$

It should be noted that $\bar{\mathbf{A}}_{\mathbf{S}}$ is a complex valued matrix so, for some solvers, it may be necessary to derive two constraints from the real and the imaginary parts.

So, finally, any optimization must be subject to the constraints defined by

$$\mathfrak{C}(\mathbf{w}) = \begin{cases} \mathbf{A}_0 \mathbf{w} & \leq \mathbf{0}_{2LZ} \\ \mathbf{A}_T \mathbf{w} & \leq N_t \cdot \mathbf{1}_Z \\ \bar{\mathbf{A}}_S \mathbf{w} & = 0 \end{cases} \quad (2.20)$$

2.2 Objective function

As mentioned at the beginning of the chapter, there are several quantities of interest depending on the harmonic content of the air gap that may be optimized in a machine. These include the maximization of the average torque, the minimization of torque ripple, losses and UMP. It is immediately apparent that all minimizations are trivially solved by a machine with no winding at all, which would not produce a fundamental harmonic (\bar{m}_p^\ominus) and therefore could not be able to make a conversion between electric and mechanic power. So the fundamental harmonic amplitude must always be included as a lower bound (LB) constraint or as an objective function.

2.3 Fundamental harmonic maximization

As seen in section 2.1, the harmonics are a linear function of the winding vector, in particular the fundamental harmonic can be calculated with (2.6) defined specifically for the fundamental component.

$$\bar{m}_p^\ominus = \bar{\mathbf{v}}_p^\ominus \mathbf{w} \quad (2.21)$$

However, the cited function is a complex function of the winding vector and its result is a phasor ($\bar{m}_p^\ominus \in \mathbb{C}$). As \mathbb{C} is not ordered, the maximum and minimum cannot be defined. What must be maximized or minimized actually is not the fundamental harmonic but its module, and unfortunately the module operator is not linear, so the linear optimization algorithms (which are extremely efficient) are not suitable to find the optimum. Nonetheless, the square module of the fundamental harmonic (or any other) can be expressed as a quadratic form.

$$\begin{aligned}
|\bar{m}_n^\oplus|^2 &= \left(\bar{m}_n^\oplus\right)^* \bar{m}_n^\oplus \\
&= \left(\bar{\mathbf{v}}_n^\oplus \mathbf{w}\right)^* \bar{\mathbf{v}}_n^\oplus \mathbf{w} \\
&= \left(\bar{\mathbf{v}}_n^\oplus\right)^* \mathbf{w} \bar{\mathbf{v}}_n^\oplus \mathbf{w} \\
&= \left[\mathbf{w}^T \left(\bar{\mathbf{v}}_n^\oplus\right)^H\right]^T \bar{\mathbf{v}}_n^\oplus \mathbf{w} \\
&= \mathbf{w}^T \left(\bar{\mathbf{v}}_n^\oplus\right)^H \bar{\mathbf{v}}_n^\oplus \mathbf{w} \\
&= \mathbf{w}^T \bar{\mathbf{H}}_n^\oplus \mathbf{w}
\end{aligned} \tag{2.22}$$

where $*$ apex represents the complex conjugate and H apex represents the complex conjugate transpose (i.e. the hermitian conjugate). Matrix $\bar{\mathbf{H}}_n$ is symmetric and complex valued but, considering that the square of the absolute value obtained in (2.22) is a real number and that \mathbf{w} is composed of real numbers, the following can be stated:

$$|\bar{m}_n^\oplus|^2 = \text{Re} \left\{ \mathbf{w}^T \bar{\mathbf{H}}_n^\oplus \mathbf{w} \right\} = \mathbf{w}^T \text{Re} \left\{ \bar{\mathbf{H}}_n^\oplus \right\} \mathbf{w} = \mathbf{w}^T \mathbf{Q}_n^\oplus \mathbf{w} \tag{2.23}$$

where $\mathbf{Q}_n^\oplus = \text{Re} \left\{ \bar{\mathbf{H}}_n^\oplus \right\}$ is a symmetric real valued matrix of dimension $(2LZ \times 2LZ)$.

So, finally, considering that the harmonic amplitudes are real non-negative numbers by definition and that the square function is monotone over a non-negative domain, an optimization on the amplitude has the same solution as an optimization over its square value. So if the objective function is defined as

$$|\bar{m}_p^\ominus|^2 = \mathbf{w}^T \mathbf{Q}_p^\ominus \mathbf{w} \tag{2.24}$$

and the constraints as in (2.20), the solution is valid for the amplitude of the fundamental harmonic too.

It is important to notice that if the fundamental optimization is applied to a conventional configuration, for which the method of stars of slots is applicable (i.e. when Z and p comply with (1.3)), the same winding is obtained from the optimization and the star-of-slots methods. In other words, it can be said that the star of slots algorithm is already optimal for the fundamental amplitude. It is therefore licit to consider the star-of-slots windings as a reference for conventional configurations, when

other optimizations are applied sacrificing part of the fundamental. If also non-conventional configurations (not complying with (1.3)) are taken into account, a wider set of feasible windings is obtained. By applying the fundamental optimization to obtain the unconventional winding, the result can be considered as a reference for further optimizations, as the star of slots is considered as a reference for the conventional configuration.

As an example, the winding matrix obtained by the fundamental maximization for a five teeth ($Z = 5$), four poles ($p = 2$) and three phases ($L = 3$) machine is shown in Tab. 2.1, where some characteristics of unconventional windings can be noticed.

Table 2.1: Example of winding matrix \mathbf{W} (highlighted in blue), obtained for the 5 – 4 configuration with $L = 3$

$k \backslash l$	0	1	2	3	4	5
0	0	88.55	11.44	0	0	0
1	0	0	0	33.82	66.17	0
2	100	0	0	0	0	0
3	0	0	66.17	33.82	0	0
4	0	0	0	0	11.44	88.55

First, as the optimization is operated on a continuous domain, the calculated number of turns is not integer. Furthermore, the three phases have different distribution, meaning that the pattern of the first phase is different from the one of the other two, but also they do not feature the same total number of turns (167.65 for the first phase and 166.17 for the other two). Nevertheless, the three phases give equal contribution to the fundamental harmonic because of the symmetry constraint.

Clearly, for the winding feasibility, the values obtained from the optimization must be rounded as in Tab. 2.2, but if the number of turns is sufficiently high the MMF contribution will be affected marginally. In this case, counter-intuitively, the winding factor of the rounded result (0.8834) is higher than the one of the optimized result (0.8829), but this is due to the fact that, strictly speaking, the rounding operation breaks the symmetry constraint.

Table 2.2: Rounded winding matrix \mathbf{W} (highlighted in blue), obtained for the 5 – 4 configuration with $L = 3$

$k \backslash l$	0	1	2	3	4	5
	A^+	C^-	B^+	A^-	C^+	B^-
0	0	89	11	0	0	0
1	0	0	0	34	66	0
2	100	0	0	0	0	0
3	0	0	66	34	0	0
4	0	0	0	0	11	89

It should be noted here that, for the conventional configurations, the solution of the maximization of the fundamental amplitude is unique, meaning that the winding matrix is always the same except for rotations of the phases, so the harmonic content does not change. Conversely, for unconventional configurations, the same maximum fundamental can be obtained for different winding matrices, having more than two non zero values for each line, showing different harmonic content (except for the fundamental of course) and different permanent magnet (PM) losses (this topic will be developed in section 2.4).

In particular, it has been observed that the matrices giving lower losses tend to have more regular layouts, with only two values per line of the matrix and showing a certain symmetry between the phases. Table 2.2 is an example: the symmetry of phase A ($l = 0, 3$) around tooth 2 is apparent, the other two phases B and C ($l = 1, 4$ and $l = 5, 2$) are specular. This fact is more evident if the classic phase notation is used.

Table 2.3: Classic phase notation of the winding matrix (highlighted in yellow), equivalent to Tab. 2.2

$k \backslash$	A	B	C
0	0	11	-89
1	-34	0	66
2	100	0	0
3	-34	66	0
4	0	-89	11

In all cases (as in Tab. 2.2) the winding matrix that appears most regular and giving the lowest losses has been used for unconventional

windings.

2.3.1 Winding selection

With this technique, a whole set of conventional and unconventional windings can be obtained, for almost any $Z - 2p$ pair. By the way not all pairs have the same performance. For example any machine having equal number of teeth and poles ($Z = 2p$) would produce zero torque when the poles face exactly the teeth. Not only this would produce a high torque ripple, but also, because of the reluctance of the stator, the cogging torque would most likely cause the rotor to stop exactly in the zero torque position, giving no starting torque.

The winding factor is another important parameter normally taken into account, as the winding factor of the fundamental harmonic is directly connected to the average torque that the machine can produce. Recalling (1.40) and (1.43) particularized for the fundamental harmonic:

$$\kappa_{wp}^{\ominus} = \kappa_{cp} \kappa_{dn}^{\ominus} \quad \kappa_{cp} = \sin\left(\frac{p}{Z}\pi\right)$$

the value of the chord factor (κ_{cp}) is maximum when $Z = 2p$, but this case has been excluded. On the other hand, all the cases in which $\frac{p}{Z}\pi = \frac{\pi}{2} + h\pi$ with $h > 0$ have a low distribution factor. So the best choice is to take a configuration for which $Z \approx 2p$ but $Z \neq 2p$. In the Tab. 2.4 the winding factors are given both for conventional and non-conventional windings, the non-conventional windings have been optimized to have the highest possible winding factor.

Table 2.4 shows the winding factors calculated for several $Z - 2p$, three phase configurations. Only the values for which $\frac{1}{4} < q < \frac{1}{2}$ are shown, as this criterion in most cases brings to an acceptable winding factor (i.e. greater than 0.7). It can be seen, the table has been truncated at 20 poles, by the way it can be noticed that the winding factors show a symmetry around a pole number $2p = Z$ (highlighted by the black line) so the eliminated values can be deduced by the lower pole number values.

Defining $\kappa_w(Z, 2p)$ the winding factor obtained for $2p$ poles and Z teeth,

$$\kappa_w(Z, Z - r) = \kappa_w(Z, Z + r) \quad (2.25)$$

Table 2.4: Winding factor, obtained for various $Z - 2p$ combinations and three phases ($L = 3$), only the values for which $\frac{1}{4} < q < \frac{1}{2}$ are shown, unconventional configurations are shaded.

$Z \backslash 2p$	2	4	6	8	10	12	14	16	18	20
3	0.866	0.866								
4	0.549		0.549							
5	0.546	0.883	0.883							
6		0.866		0.866						
7		0.736	0.918	0.918	0.736					
8		0.549	0.844		0.844					
9			0.866	0.945	0.945	0.866				
10			0.751	0.883		0.883	0.751			
11			0.718	0.864	0.940	0.940	0.864			
12				0.866	0.933		0.933	0.866		
13				0.783	0.889	0.944	0.944	0.889	0.783	
14				0.736	0.848	0.918		0.918	0.848	
15					0.866	0.883	0.951	0.951	0.883	0.866
16					0.785	0.844	0.926		0.926	0.844
17					0.760	0.853	0.916	0.949	0.949	0.916
18					0.735	0.866	0.902	0.945		0.945
⋮										
21						0.747	0.866	0.890	0.918	0.953

where r is any even or odd natural number respectively if Z is odd or even.

2.4 Permanent magnet losses minimization

FSCW windings are known to be affected by large MMF harmonics which produce eddy current losses in the rotor permanent magnets. While the losses in the magnets may be marginally relevant from the efficiency point of view, the rare earth magnets are known to be particularly vulnerable to high temperatures and the eddy currents induced in the magnets can be responsible for overheating. Exploiting the possibility to modify the harmonic content generated by the stator, it is possible to modify the

ratio between the fundamental harmonic and other harmonics that generate losses.

It has been shown [1] that each harmonic produces losses proportional to its square amplitude and that the harmonic losses are independent of each other, meaning that the total eddy current losses can be obtained by the sum of the losses of each harmonic calculated separately. The weight of harmonic \bar{m}_n^\oplus will be referred to as y_n^\oplus so that its produced losses will be

$$Y_n^\oplus = y_n^\oplus |\bar{m}_n^\oplus|^2 \quad (2.26)$$

and the total losses will be

$$Y = \sum_n (Y_n^\ominus + Y_n^\oplus) \quad n = 1, 2, \dots \quad (2.27)$$

It may be noted that in this expression y_p^\ominus must be zero, as \bar{m}_p^\ominus is synchronous with the rotor, and therefore it cannot induce eddy currents.

By substituting (2.23) and (2.26) into (2.27), it is possible to consider the total losses as a quadratic function of the winding vector \mathbf{w} .

$$\begin{aligned} Y(\mathbf{w}) &= \sum_n (y_n^\ominus |\bar{m}_n^\ominus|^2 + y_n^\oplus |\bar{m}_n^\oplus|^2) \\ &= \sum_n (y_n^\ominus \mathbf{w}^T \mathbf{Q}_n^\ominus \mathbf{w} + y_n^\oplus \mathbf{w}^T \mathbf{Q}_n^\oplus \mathbf{w}) \\ &= \mathbf{w}^T \sum_n (y_n^\ominus \mathbf{Q}_n^\ominus + y_n^\oplus \mathbf{Q}_n^\oplus) \mathbf{w} \\ &= \mathbf{w}^T \mathbf{Q}_{\text{harm}} \mathbf{w} \end{aligned} \quad (2.28)$$

where $\mathbf{Q}_{\text{harm}} = \sum_n (y_n^\ominus \mathbf{Q}_n^\ominus + y_n^\oplus \mathbf{Q}_n^\oplus)$ is the square matrix taking into account the contributions to the losses by all the harmonics.

At this point we have two objectives for the problem defined by the maximum fundamental (2.24) and the minimum losses (2.28), which lead to different solutions. To calculate both the optimizations as a minimization, the two objective functions will be

$$\mathfrak{F}_{\text{loss}}(\mathbf{w}) = \mathbf{w}^T \mathbf{Q}_{\text{harm}} \mathbf{w} \quad (2.29a)$$

$$\mathfrak{F}_{\text{fund}}(\mathbf{w}) = -[\mathbf{w}^T \mathbf{Q}_p^\ominus \mathbf{w}] \quad (2.29b)$$

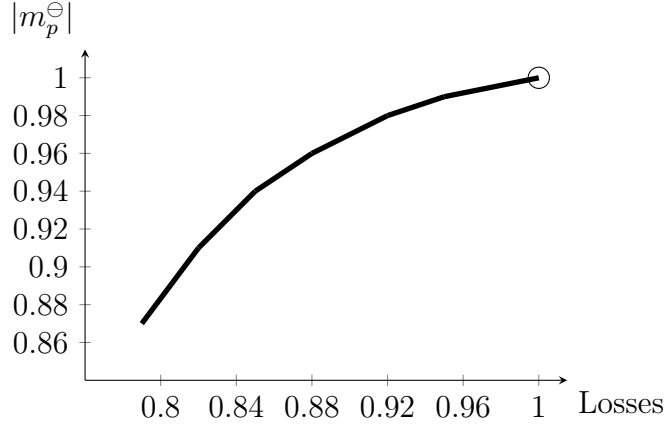


FIGURE 2.1: Example on a per-unit base of a Pareto curve obtained from the fundamental maximization (highlighted by \circ) and gradually reducing the fundamental to allow the losses minimization

A common way to combine the two objectives into a single multi-objective function \mathfrak{F} is to sum the two functions assigning them two complementary weights as in (2.30),

$$\mathfrak{F}(\mathbf{w}) = (a) \mathfrak{F}_{fund}(\mathbf{w}) + (1 - a) \mathfrak{F}_{loss}(\mathbf{w}) \quad \text{with} \quad a \in [0, 1] \quad (2.30)$$

which gives a single quadratic function with linear constraints. Theoretically, moving a in its range, a Pareto frontier is drawn on a fundamental amplitude against losses plane (Fig. 2.1).

Because in some cases the optimization turned out to be too sensitive to the variations of the weight parameter a to obtain a continuous Pareto curve, an alternative way to obtain the curve can be used. The starting point is set by the winding obtained by the maximization of the fundamental amplitude alone, corresponding to (2.29b) or to $a = 1$ in (2.30). The obtained value of the maximum fundamental will be referred to as m_{\max} .

The following points are obtained using as objective function only the loss function (2.29a), whose absolute minimum is trivially found with an empty winding, giving no losses. To avoid the trivial solution, a lower bound for the fundamental amplitude is fixed below the maximum value $LB = a m_{\max}$. A sequence of constrained minima along the Pareto curve can be found using a sequence of decreasing lower bound constraints on

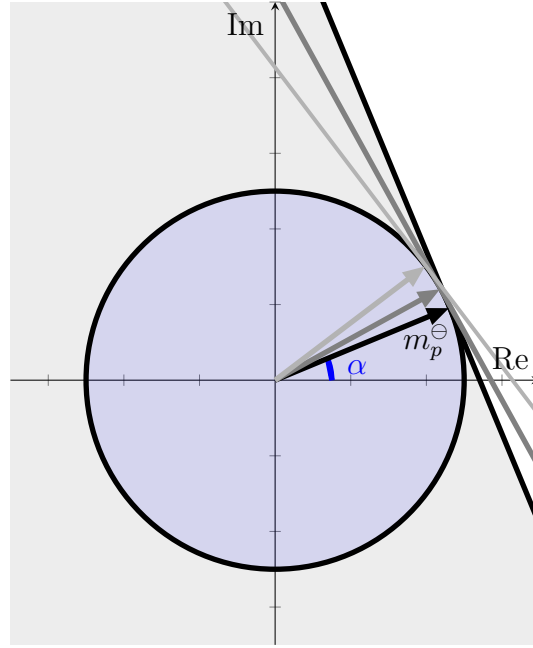


FIGURE 2.2: Representation of a series of linear lower bound optimizations whose envelope coincides with a quadratic lower bound optimization

the fundamental amplitude:

$$\text{LB} \leq |\bar{m}_p^\ominus| \quad (2.31)$$

Unfortunately, the condition on the absolute value of the phasor defined by (2.31) would be a quadratic constraint but in quadratic programming the constraints must be linear. This problem can be overcome defining a set of linear lower bounds (2.33) whose envelope coincides with the circumference defined by LB.

$$\text{LB} < \cos(\alpha) \text{Re}(\bar{m}_p^\ominus) + \sin(\alpha) \text{Im}(\bar{m}_p^\ominus) \quad (2.32)$$

which can be expressed as a linear function of \mathbf{w}

$$\text{LB} < [\cos(\alpha) \text{Re}(\bar{\mathbf{v}}_p^\ominus) + \sin(\alpha) \text{Im}(\bar{\mathbf{v}}_p^\ominus)] \mathbf{w} \quad (2.33)$$

In Fig. 2.2, the linear constraints are represented varying α so that they are tangential to the circumference defined by $|\bar{m}_p^\ominus| = \text{LB}$, the region filled in blue represents (2.31), while the region filled in grey (including the blue region) represents (2.33).

Each optimization complying with a linear constraint certainly complies with the underlying quadratic constraint given by the lower bound module of the fundamental harmonic. A quasi-optimum is obtained from the minimum among all the linearly constrained minima.

In Fig. 2.3 the reduction of the losses can be seen. The star-of-slots winding is taken as reference, the optimized winding features a decrease of the losses by the 25.8% with a decrease of the fundamental by the 2%, a decrease of the fundamental by the 4% brings a losses decrease by the 35%. By the way it can be seen, from the ratio between losses and the square of the fundamental, that pushing the optimization beyond the 4% of fundamental decrease, the losses decrease is mainly due to the fundamental itself (or rather of m_5^\oplus that is linked to the fundamental). finally, the reducible harmonics are reduced to 0 when the fundamental is reduced by the 9%

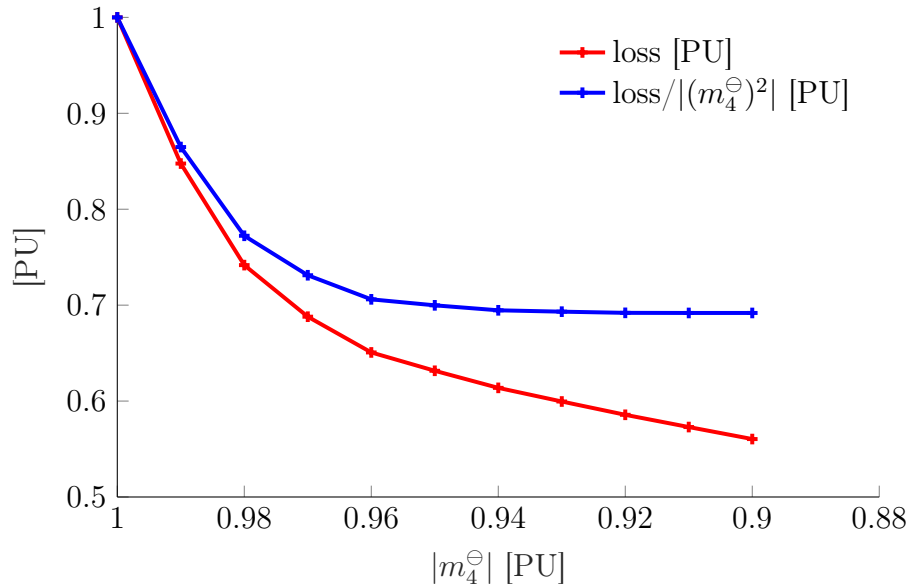


FIGURE 2.3: Losses (red) ratio between losses and the square of the fundamental (blue)

The result of the minimization on the harmonics can be seen in Fig. 2.4, showing respectively the conventional star of slots winding design and the optimized winding design. On the left ((a) and (c)) there is the winding matrix in the classical phase notation, and on the right ((b) and (d)) the spectra, limited to the first Z harmonics.

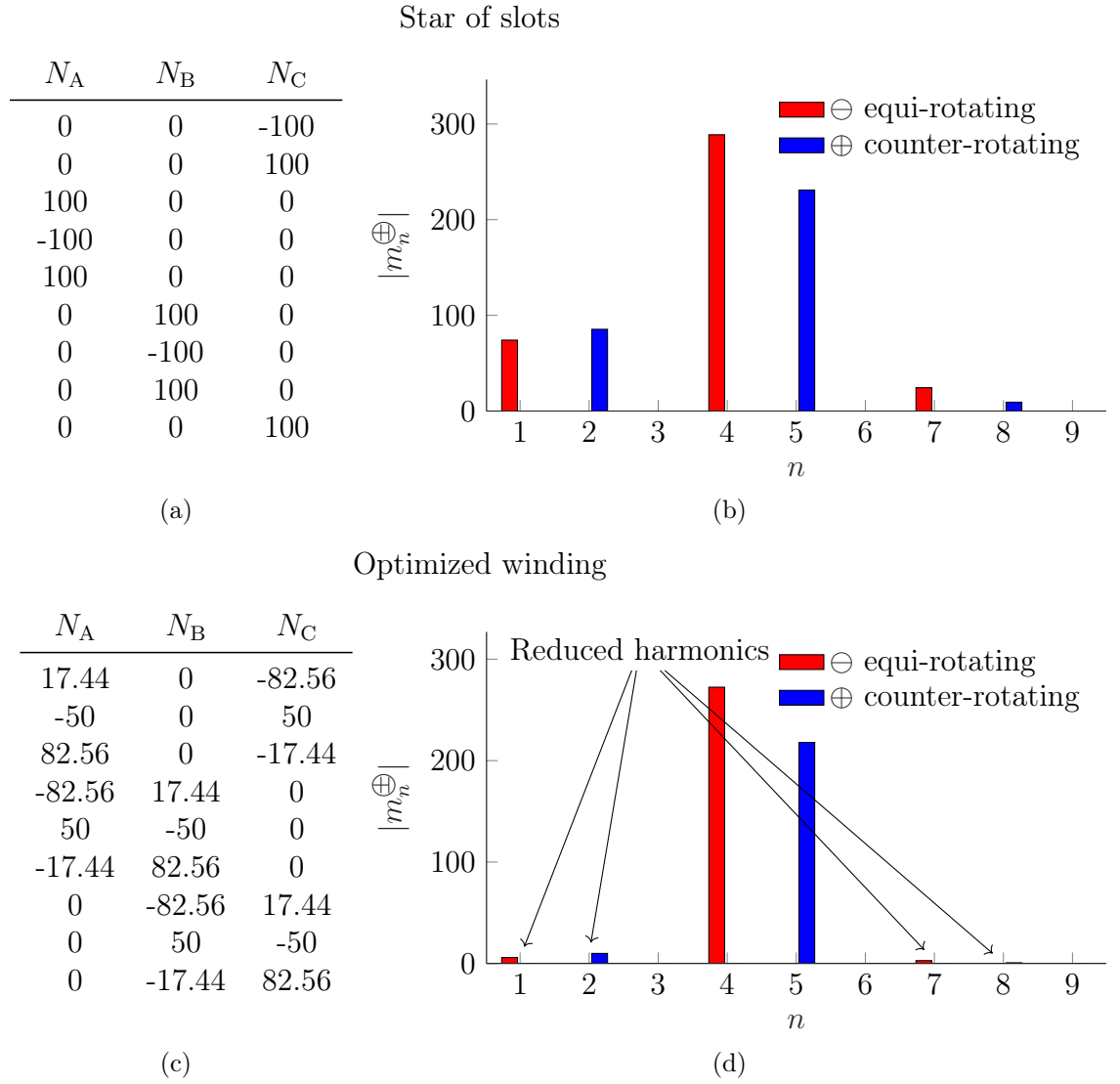


FIGURE 2.4: Reduction of the harmonics causing losses on the 9 – 8 configuration, (a) and (c) classic notation winding matrix, (b) and (d) spectra

For the calculation of the harmonic losses, the formulas in [1] have been used and, for the sake of completeness, they are reported hereafter. The computed losses are given in table Tab. 2.5. The results, obtained analytically, are confirmed by FEA simulations [1].

$$\begin{aligned}
y_n^\oplus &= \frac{4\pi\mu_0^2 n^2 L \omega_n^{\pm 2} \sigma}{R_{\text{mag}}^4 R_s^2 \left| \Delta_n^\oplus \right|^2} \int_{R_R}^{R_{\text{mag}}} \left| \varepsilon_n^\oplus Y_n \left(\kappa_n^\oplus r \right) - \varphi_n^\oplus J_n \left(\kappa_n^\oplus r \right) \right|^2 r dr \\
\delta_n^\oplus &= -\kappa_n^\oplus Y_{n+1} \left(\kappa_n^\oplus R_{\text{mag}} \right) + n R_{\text{mag}}^{-1} Y_n \left(\kappa_n^\oplus R_{\text{mag}} \right) \\
\varepsilon_n^\oplus &= \kappa_n^\oplus J_{n+1} \left(\kappa_n^\oplus R_R \right) - n R_R^{-1} J_n \left(\kappa_n^\oplus R_R \right) \\
\varphi_n^\oplus &= \kappa_n^\oplus Y_{n+1} \left(\kappa_n^\oplus R_R \right) - n R_R^{-1} Y_n \left(\kappa_n^\oplus R_R \right) \\
\kappa_n^\oplus &= \sqrt{-j\sigma\mu\omega_n^\oplus} = (1-j)\sqrt{\sigma\mu\omega_n^\oplus/2} \\
\Delta_n^\oplus &= \left(\beta_n^\oplus \varepsilon_n^\oplus - \alpha_n^\oplus \varphi_n^\oplus - j\delta_n^\oplus \varepsilon_n^\oplus + j\chi_n^\oplus \varphi_n^\oplus \right) R_s^{n-1} R_{\text{mag}}^{-n-1} \\
&\quad + \left(\alpha_n^\oplus \varphi_n^\oplus - \beta_n^\oplus \varepsilon_n^\oplus - j\delta_n^\oplus \varepsilon_n^\oplus + j\chi_n^\oplus \varphi_n^\oplus \right) R_{\text{mag}}^{n-1} R_s^{-n-1} \\
\alpha_n^\oplus &= jn J_n \left(\kappa_n^\oplus R_{\text{mag}} \right) R_{\text{mag}}^{-1} \\
\beta_n^\oplus &= -jn Y_n \left(\kappa_n^\oplus R_{\text{mag}} \right) R_{\text{mag}}^{-1} \\
\chi_n^\oplus &= -\kappa_n^\oplus J_{n+1} \left(\kappa_n^\oplus R_{\text{mag}} \right) + n R_{\text{mag}}^{-1} J_n \left(\kappa_n^\oplus R_{\text{mag}} \right)
\end{aligned}$$

Where R_R , R_{mag} and R_s represent respectively the radius at the iron surface of the rotor, the radius at the surface of the magnets towards the air gap and the bore radius of the stator. Y_n and J_n represent the n^{th} order Bessel functions of the first and second kind.

Table 2.5: Specific losses expressed in mW/mm^3 calculated for various $Z - 2p$ combinations. The unconventional configurations are shaded.

$Z \backslash 2p$	2	4	6	8	10	12	14	16	18	20
3	0.18	7.81								
4	0.07		20.63							
5	0.04	0.36	3.42							
6		0.17		7.73						
7		0.11	0.55	2.47	13.81					
8		0.06	0.26		4.58					
9			0.16	0.79	2.17	7.60				
10			0.11	0.33		3.33	11.48			
11			0.13	0.24	0.69	1.79	5.46			
12				0.15	0.58		2.88	7.51		
13				0.12	0.34	0.72	1.64	4.04	10.61	
14				0.09	0.19	0.49		2.35	5.71	
15					0.14	0.29	0.79	1.56	3.12	7.41
16					0.11	0.22	0.53		2.02	4.28
17					0.13	0.18	0.45	0.74	1.39	2.82
18						0.13	0.38	0.72		2.01

2.5 Unbalanced magnetic pull analysis and minimization

In general, in rotating electrical machines, the magnetic flux in the air gap between stator and the rotor produces a surface force density with both a tangential and a normal component. If the net result of the surface forces is not zero, the net force will be called Unbalanced Magnetic Pull (UMP).

There may be several causes for the UMP in an electrical machine, mechanical eccentricity, that has been studied from the beginning of the 20th century to nowadays [2] [3] [4], being the most well known.

In the case that rotor and stator have an eccentricity, the reduced air gap on one side will induce a larger flux density compared to the opposite side. If they maintain their reciprocal positions a static pull arises[5]. Conversely, an eccentricity due to rotor bending leads to a

dynamic UMP [6] (and therefore vibrations) and vice versa [7]. It is also known that electrical faults [8] can cause dynamic UMP.

Excluding mechanical or electrical anomalies, it is known that for some particular slot-pole configurations, FSCW machines are affected by an UMP due to the interaction of induction space harmonics. In this section an explanation of the relation between the harmonic content of the air gap and the UMP will be given to identify the configurations affected by UMP.

2.5.1 Magnetic interaction between stator and rotor

The Maxwell stress tensor is commonly used to evaluate electromagnetic forces; the general form can be found in [9]. For the sake of calculating the UMP in electrical machines, in most cases a simplified 2D model is adequate; in this case the stress tensor can be used in its simplified form [10].

$$\mathbf{F} = \frac{1}{2\mu_0} \iint_S [(B_n^2 - B_t^2)\hat{\mathbf{n}} + 2(B_n B_t)\hat{\mathbf{t}}] dS \quad (2.34)$$

where $\hat{\mathbf{n}}$ and $\hat{\mathbf{t}}$ are respectively the normal and tangential unit vectors, “n” and “t” subscripts indicate the normal and tangential components of the flux density (B) and S is a cylindrical surface separating the rotor and the stator. The normal component of the force is referred to as magnetic pressure and the tangential component as magnetic tension.

A further simplification is commonly used to calculate the force between stator and rotor, if the tangential component of the magnetic flux density is negligible, (2.34) is reduced to

$$\mathbf{F} = \frac{1}{2\mu_0} \iint_S B_n^2 \hat{\mathbf{n}} dS \quad (2.35)$$

It is well known that UMP is caused by the interaction of two field space harmonics differing by one order. It also known that, in conventional windings, there cannot be two harmonics of the same order rotating in opposite directions and, if there are two neighbour harmonics, they must rotate in opposite directions [11]. Considering a non-saturated machine with constant air gap, the normal component of the flux density

(B_n) can be considered proportional to the MMF, therefore the harmonic analysis developed in chapter 1 can be used.

$$F_x(t) = \frac{\mu_0}{2g^2} \int_0^{2\pi} [\text{Re}(\bar{M}(\theta, t))]^2 \cos(\theta) L_{\text{ax}} R_{\text{gap}} d\theta \quad (2.36a)$$

$$F_y(t) = \frac{\mu_0}{2g^2} \int_0^{2\pi} [\text{Re}(\bar{M}(\theta, t))]^2 \sin(\theta) L_{\text{ax}} R_{\text{gap}} d\theta \quad (2.36b)$$

where L_{ax} is the axial length of the machine, R_{r} , $R_{\text{gap}} = \frac{R_{\text{r}} + R_{\text{s}}}{2}$ and R_{s} are respectively the rotor iron surface radius, the mid-gap radius and the stator bore radius.

2.5.2 Harmonics causing dynamic UMP

As stated before, the UMP can be divided in static and dynamic components. In this paragraph the components will be separated and the dynamic component will be explored in detail as it is the one responsible for vibrations and noise.

From (2.36a), the following can be obtained substituting (1.19) (the same procedure can be applied to (2.36b) analogously)

$$F_x(t) = \frac{\mu_0 L_{\text{ax}} R_{\text{gap}}}{2g^2} \int_0^{2\pi} \left\{ \sum_{n=0}^{\infty} \text{Re} [e^{j(\omega t - n\theta)} \bar{m}_n^{\ominus} + e^{j(\omega t + n\theta)} \bar{m}_n^{\oplus}] \right\}^2 \cos(\theta) d\theta \quad (2.37)$$

The square component of the integrand can be expressed as follows

$$\begin{aligned} & \left\{ \sum_{n=0}^{\infty} \text{Re} [e^{j(\omega t - n\theta)} \bar{m}_n^{\ominus} + e^{j(\omega t + n\theta)} \bar{m}_n^{\oplus}] \right\}^2 \\ &= \sum_{n=0}^{\infty} \text{Re} [e^{j(\omega t - n\theta)} \bar{m}_n^{\ominus} + e^{j(\omega t + n\theta)} \bar{m}_n^{\oplus}] \sum_{n'=0}^{\infty} \text{Re} [e^{j(\omega t - n'\theta)} \bar{m}_{n'}^{\ominus} + e^{j(\omega t + n'\theta)} \bar{m}_{n'}^{\oplus}] \\ &= \frac{1}{4} \sum_{n=0}^{\infty} \left[e^{j(\omega t - n\theta)} \bar{m}_n^{\ominus} + e^{j(\omega t + n\theta)} \bar{m}_n^{\oplus} + \right. \\ & \quad \left. e^{-j(\omega t - n\theta)} \bar{m}_n^{\ominus*} + e^{-j(\omega t + n\theta)} \bar{m}_n^{\oplus*} \right] \sum_{n'=0}^{\infty} \left[e^{j(\omega t - n'\theta)} \bar{m}_{n'}^{\ominus} + e^{j(\omega t + n'\theta)} \bar{m}_{n'}^{\oplus} + \right. \\ & \quad \left. e^{-j(\omega t - n'\theta)} \bar{m}_{n'}^{\ominus*} + e^{-j(\omega t + n'\theta)} \bar{m}_{n'}^{\oplus*} \right] \end{aligned}$$

developing the products

$$= \frac{1}{4} \sum_{n=0}^{\infty} \sum_{n'=0}^{\infty} \left[\begin{aligned} & e^{j(\omega t - n\theta)} \bar{m}_n^{\ominus} e^{j(\omega t - n'\theta)} \bar{m}_{n'}^{\ominus} + e^{j(\omega t + n\theta)} \bar{m}_n^{\oplus} e^{j(\omega t - n'\theta)} \bar{m}_{n'}^{\ominus} + \\ & e^{j(\omega t - n\theta)} \bar{m}_n^{\ominus} e^{j(\omega t + n'\theta)} \bar{m}_{n'}^{\oplus} + e^{j(\omega t + n\theta)} \bar{m}_n^{\oplus} e^{j(\omega t + n'\theta)} \bar{m}_{n'}^{\oplus} + \\ & e^{j(\omega t - n\theta)} \bar{m}_n^{\ominus} e^{-j(\omega t - n'\theta)} \bar{m}_{n'}^{\ominus*} + e^{j(\omega t + n\theta)} \bar{m}_n^{\oplus} e^{-j(\omega t - n'\theta)} \bar{m}_{n'}^{\ominus*} + \\ & e^{j(\omega t - n\theta)} \bar{m}_n^{\ominus} e^{-j(\omega t + n'\theta)} \bar{m}_{n'}^{\oplus*} + e^{j(\omega t + n\theta)} \bar{m}_n^{\oplus} e^{-j(\omega t + n'\theta)} \bar{m}_{n'}^{\oplus*} + \\ & e^{-j(\omega t - n\theta)} \bar{m}_n^{\ominus*} e^{j(\omega t - n'\theta)} \bar{m}_{n'}^{\ominus} + e^{-j(\omega t + n\theta)} \bar{m}_n^{\oplus*} e^{j(\omega t - n'\theta)} \bar{m}_{n'}^{\ominus} + \\ & e^{-j(\omega t - n\theta)} \bar{m}_n^{\ominus*} e^{j(\omega t + n'\theta)} \bar{m}_{n'}^{\oplus} + e^{-j(\omega t + n\theta)} \bar{m}_n^{\oplus*} e^{j(\omega t + n'\theta)} \bar{m}_{n'}^{\oplus} + \\ & e^{-j(\omega t - n\theta)} \bar{m}_n^{\ominus*} e^{-j(\omega t - n'\theta)} \bar{m}_{n'}^{\ominus*} + e^{-j(\omega t + n\theta)} \bar{m}_n^{\oplus*} e^{-j(\omega t - n'\theta)} \bar{m}_{n'}^{\ominus*} + \\ & e^{-j(\omega t - n\theta)} \bar{m}_n^{\ominus*} e^{-j(\omega t + n'\theta)} \bar{m}_{n'}^{\oplus*} + e^{-j(\omega t + n\theta)} \bar{m}_n^{\oplus*} e^{-j(\omega t + n'\theta)} \bar{m}_{n'}^{\oplus*} \end{aligned} \right]$$

Reorganizing the exponentials

$$= \frac{1}{4} \sum_{n=0}^{\infty} \sum_{n'=0}^{\infty} \left[\begin{aligned} & e^{j(2\omega t - (n+n')\theta)} \bar{m}_n^{\ominus} \bar{m}_{n'}^{\ominus} + e^{-j(2\omega t - (n+n')\theta)} \bar{m}_n^{\ominus*} \bar{m}_{n'}^{\ominus*} + \\ & e^{j(2\omega t + (n-n')\theta)} \bar{m}_n^{\oplus} \bar{m}_{n'}^{\oplus} + e^{-j(2\omega t + (n-n')\theta)} \bar{m}_n^{\oplus*} \bar{m}_{n'}^{\oplus*} + \\ & e^{j(2\omega t - (n-n')\theta)} \bar{m}_n^{\ominus} \bar{m}_{n'}^{\oplus} + e^{-j(2\omega t - (n-n')\theta)} \bar{m}_n^{\ominus*} \bar{m}_{n'}^{\oplus*} + \\ & e^{j(2\omega t + (n+n')\theta)} \bar{m}_n^{\oplus} \bar{m}_{n'}^{\oplus} + e^{-j(2\omega t + (n+n')\theta)} \bar{m}_n^{\oplus*} \bar{m}_{n'}^{\oplus*} + \\ & e^{j(-(n-n')\theta)} \bar{m}_n^{\ominus} \bar{m}_{n'}^{\ominus*} + e^{j((n+n')\theta)} \bar{m}_n^{\oplus} \bar{m}_{n'}^{\oplus*} + \\ & e^{j(-(n+n')\theta)} \bar{m}_n^{\ominus} \bar{m}_{n'}^{\oplus*} + e^{j((n-n')\theta)} \bar{m}_n^{\oplus} \bar{m}_{n'}^{\ominus*} + \\ & e^{j((n-n')\theta)} \bar{m}_n^{\ominus*} \bar{m}_{n'}^{\ominus} + e^{j(-(n+n')\theta)} \bar{m}_n^{\oplus*} \bar{m}_{n'}^{\oplus} + \\ & e^{j((n+n')\theta)} \bar{m}_n^{\ominus*} \bar{m}_{n'}^{\oplus} + e^{j(-(n-n')\theta)} \bar{m}_n^{\oplus*} \bar{m}_{n'}^{\oplus} \end{aligned} \right] \quad (2.38)$$

The dynamic terms of the sum (having $2\omega t$) can be clearly distinguished from the static terms, in which ωt is not present; it can be observed that the dynamic components have a double frequency with respect to the electric frequency.

Considering that the integrand of (2.37) contains $\cos(\theta) = \frac{1}{2}(e^{j\theta} + e^{-j\theta})$ and considering only the dynamic component from (2.38), the integrand of the dynamic component can be expressed as

$$\frac{1}{8} \sum_{n=0}^{\infty} \sum_{n'=0}^{\infty} \begin{bmatrix} e^{j(2\omega t - (n+n')\theta)} \bar{m}_n^{\ominus} \bar{m}_{n'}^{\ominus} + e^{-j(2\omega t - (n+n')\theta)} \bar{m}_n^{\ominus*} \bar{m}_{n'}^{\ominus*} + \\ e^{j(2\omega t + (n-n')\theta)} \bar{m}_n^{\oplus} \bar{m}_{n'}^{\ominus} + e^{-j(2\omega t + (n-n')\theta)} \bar{m}_n^{\oplus*} \bar{m}_{n'}^{\ominus*} + \\ e^{j(2\omega t - (n-n')\theta)} \bar{m}_n^{\ominus} \bar{m}_{n'}^{\oplus} + e^{-j(2\omega t - (n-n')\theta)} \bar{m}_n^{\ominus*} \bar{m}_{n'}^{\oplus*} + \\ e^{j(2\omega t + (n+n')\theta)} \bar{m}_n^{\oplus} \bar{m}_{n'}^{\oplus} + e^{-j(2\omega t + (n+n')\theta)} \bar{m}_n^{\oplus*} \bar{m}_{n'}^{\oplus*} \end{bmatrix} \cdot (e^{j\theta} + e^{-j\theta}) \quad (2.39)$$

It should be noted that, in the exponent, the sign of n and n' is related to the rotation sense of the correspondent harmonics, meaning that if the correspondent harmonics rotate in the same direction, n and n' have the same sign; if the correspondent harmonics rotate the opposite way, n and n' have the opposite sign. Now, developing the product in (2.39), we obtain the following expression of the integrand:

$$\frac{1}{8} \sum_{n=0}^{\infty} \sum_{n'=0}^{\infty} \begin{bmatrix} e^{j(2\omega t - (n+n'+1)\theta)} \bar{m}_n^{\ominus} \bar{m}_{n'}^{\ominus} + e^{-j(2\omega t - (n+n'+1)\theta)} \bar{m}_n^{\ominus*} \bar{m}_{n'}^{\ominus*} + \\ e^{j(2\omega t + (n-n'+1)\theta)} \bar{m}_n^{\oplus} \bar{m}_{n'}^{\ominus} + e^{-j(2\omega t + (n-n'+1)\theta)} \bar{m}_n^{\oplus*} \bar{m}_{n'}^{\ominus*} + \\ e^{j(2\omega t - (n-n'+1)\theta)} \bar{m}_n^{\ominus} \bar{m}_{n'}^{\oplus} + e^{-j(2\omega t - (n-n'+1)\theta)} \bar{m}_n^{\ominus*} \bar{m}_{n'}^{\oplus*} + \\ e^{j(2\omega t + (n+n'+1)\theta)} \bar{m}_n^{\oplus} \bar{m}_{n'}^{\oplus} + e^{-j(2\omega t + (n+n'+1)\theta)} \bar{m}_n^{\oplus*} \bar{m}_{n'}^{\oplus*} + \\ e^{j(2\omega t - (n+n'-1)\theta)} \bar{m}_n^{\ominus} \bar{m}_{n'}^{\ominus} + e^{-j(2\omega t - (n+n'-1)\theta)} \bar{m}_n^{\ominus*} \bar{m}_{n'}^{\ominus*} + \\ e^{j(2\omega t + (n-n'-1)\theta)} \bar{m}_n^{\oplus} \bar{m}_{n'}^{\ominus} + e^{-j(2\omega t + (n-n'-1)\theta)} \bar{m}_n^{\oplus*} \bar{m}_{n'}^{\ominus*} + \\ e^{j(2\omega t - (n-n'-1)\theta)} \bar{m}_n^{\ominus} \bar{m}_{n'}^{\oplus} + e^{-j(2\omega t - (n-n'-1)\theta)} \bar{m}_n^{\ominus*} \bar{m}_{n'}^{\oplus*} + \\ e^{j(2\omega t + (n+n'-1)\theta)} \bar{m}_n^{\oplus} \bar{m}_{n'}^{\oplus} + e^{-j(2\omega t + (n+n'-1)\theta)} \bar{m}_n^{\oplus*} \bar{m}_{n'}^{\oplus*} \end{bmatrix} \quad (2.40)$$

Because of the linearity of the integral, the force can be split in a sum of integrals. For instance, considering generically that all terms in (2.40) contain the product of two harmonic phasors, whose value can be indicated as $\bar{m}_n^{\ominus} \bar{m}_{n'}^{\ominus} = \beta e^{j\alpha}$, (and $\bar{m}_n^{\ominus} \bar{m}_{n'}^{\ominus} = \beta e^{-j\alpha}$) the component of the force referred to the first line of (2.40) will be

$$\begin{aligned}
F_{1x} &= \frac{\mu_0 L_{\text{ax}} R_{\text{gap}}}{8g^2} \int_0^{2\pi} e^{j(2\omega t - (n+n'+1)\theta)} \bar{m}_n^\ominus \bar{m}_{n'}^\ominus + \\
&\quad e^{-j(2\omega t - (n+n'+1)\theta)} \bar{m}_n^{\ominus*} \bar{m}_{n'}^{\ominus*} d\theta \\
&= \frac{\mu_0 L_{\text{ax}} R_{\text{gap}}}{8g^2} \int_0^{2\pi} e^{j(2\omega t - (n+n'+1)\theta + \alpha)} \beta + \\
&\quad e^{-j(2\omega t - (n+n'+1)\theta + \alpha)} \beta d\theta \tag{2.41} \\
&= \frac{\mu_0 L_{\text{ax}} R_{\text{gap}}}{8g^2} \int_0^{2\pi} 2 \cos(2\omega t - (n+n'+1)\theta + \alpha) \beta d\theta \\
&= \frac{\mu_0 L_{\text{ax}} R_{\text{gap}} \beta}{4g^2} \int_0^{2\pi} \cos(2\omega t - (n+n'+1)\theta + \alpha) d\theta
\end{aligned}$$

where $\bar{m}_n^\ominus \bar{m}_{n'}^\ominus = \beta * e^{j\alpha}$

As it can be seen from (2.41), the force depends on n and n' and on the product of the amplitudes of the respective harmonics β . Now, considering $n'' \in \mathbb{Z}$ the generic coefficient of θ , the force component of any line would have the following form

$$\frac{\mu_0 L_{\text{ax}} R_{\text{gap}} \beta}{8g^2} \int_0^{2\pi} \cos(2\omega t + n''\theta + \alpha) d\theta \tag{2.42}$$

The result of the integral in (2.42) depends on $n'' \in \mathbb{Z}$ meaning that

$$\int_0^{2\pi} \cos(2\omega t + n''\theta + \alpha) d\theta = \begin{cases} 0 & \text{if } n'' \neq 0 \\ 2\pi * \cos(2\omega t + \alpha) & \text{if } n'' = 0 \end{cases} \tag{2.43}$$

This means that the net force resulting from two harmonics for which $n'' \neq 0$ is always zero. The cases in which the n'' is zero are now examined:

$$\begin{aligned}
n'' = n + n' + 1 &= 0 \text{ impossible for } n, n' \in \mathbb{N} \\
n'' = n + n' - 1 &= 0 \text{ impossible for } n, n' \in \mathbb{N} \\
n'' = n - n' + 1 &= 0 \Rightarrow n = n' - 1 \quad n \text{ and } n' \text{ opposite way} \\
n'' = n - n' - 1 &= 0 \Rightarrow n = n' + 1 \quad n \text{ and } n' \text{ opposite way}
\end{aligned} \tag{2.44}$$

From (2.44) it can be seen that the harmonics causing dynamic pull must belong to pairs of neighbour orders (differing by one) and rotating in opposite senses. Based on this result, it is simple to identify the harmful

harmonics in the spectrum of the machine. As an example, the spectrum of the 6 – 4 machine is shown. In this case all harmonics are separated so no UMP arises.

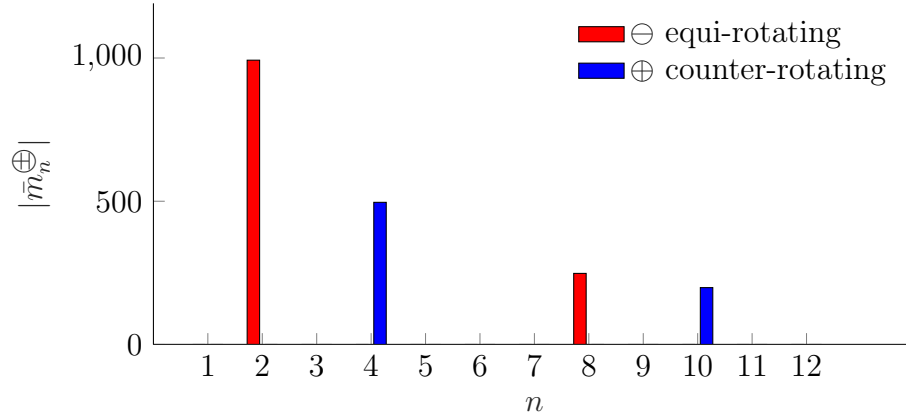


FIGURE 2.5: Amplitudes of the harmonics for the conventional 6 – 4 configuration, in red the harmonics rotating anticlockwise as the fundamental, in blue the harmonics rotating clockwise.

If the spectrum of the 9 – 8 machine of Fig. 1.4 is considered, harmonics 3, 6, 9, ... are not present, all the remaining ones differ by one order and rotate in opposite directions.

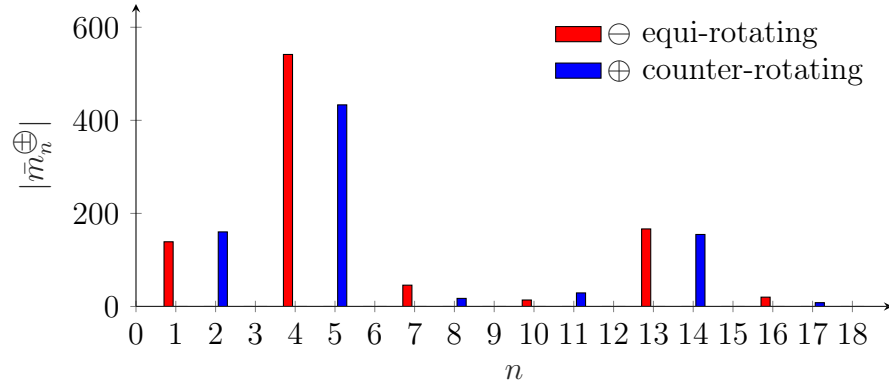


FIGURE 2.6: Amplitude of the harmonics for the conventional 9 – 8 configuration, in red the harmonics rotating anticlockwise as the fundamental, in blue the harmonics rotating clockwise.

It is clear that the worst contribution is given by the pair 4 – 5. Here, as in many cases, the fundamental harmonic (4) is the highest and the pair that gives the highest product of harmonic amplitudes is the fundamental with the previous or the next. In order to reduce the main

cause of the UMP, targeting any of the two harmonics would be effective, but reducing the fundamental, as seen before, cannot be accepted.

As reducing harmonic 4 is not acceptable, the remaining option is to reduce harmonic 5, but as seen in (1.36) m_4^\ominus and m_5^\oplus , belong to the same family (as $Z = 9$ and $Z - 5 = 4$), so it is not possible to reduce one without reducing proportionally the other.

This fact, observed in the $9 - 8$ configuration, has an important consequence. It can be seen from Tab. 2.4 that the highest values of the winding factors are the ones for which $Z = 2p \pm 1$. Unfortunately, if $Z = 2p \pm 1$, the opposite rotating harmonic $p \pm 1$ near the fundamental is always present, and therefore also its magnetic pull, which cannot be reduced (because $Z - p = p \pm 1$, as states (1.36), the harmonic responsible for the pull is linked to the fundamental).

At this point the configurations $Z - 2p$ affected by a relevant UMP must be identified and, among these, which ones are good candidates for a UMP reduction through an optimization of the winding.

In Tab. 2.6, the same set considered for the winding factor in Tab. 2.4 is examined. For each configuration, the spectrum has been calculated for the independent harmonics with (1.22), and eventually the product of all neighbour opposite-rotating pairs of harmonics has been calculated, as expected, the highest product always contained the fundamental harmonic. In all cases it has been checked if the fundamental and the neighbour harmonic causing UMP were linked. When they are linked, the neighbour harmonic causing UMP cannot be reduced (without reducing proportionally the fundamental); these cases are marked by “X”; conversely, the cases in which harmonics near the fundamental can be reduced are marked by “✓”. Finally the configurations in which the fundamental is separated from the other harmonics by a zero-valued harmonic are marked by “0”. The shaded configurations are unconventional. A particular attention is given to the $21 - 16$ combination (highlighted in yellow) as it is the first conventional winding affected by UMP that can be optimized in order to reduce the UMP.

To make a realistic comparison of the UMP for the cited machines, the magnetic flux density caused by the stator and the magnets must be considered together in load conditions. To this end, for each combination $Z - 2p$, a sequence of magneto-static FEA simulations has been made in

Table 2.6: UMP analysis for various combinations of $Z - 2p$. “0” indicates null UMP, “X” indicates that there is UMP that cannot be changed by the winding, “✓” indicates that there is UMP that can be changed modifying the winding.
The unconventional configurations are shaded, highlighted in yellow the 21 – 16 combination

$Z \backslash 2p$	2	4	6	8	10	12	14	16	18	20	22
3	X	X									
4	0		0								
5	✓	X	X								
6		0		0							
7		✓	X	X	✓						
8		0	0		0						
9			0	X	X	0					
10			0	0		0	0				
11			✓	✓	X	X	✓				
12				0	0		0	0			
13				✓	✓	X	X	✓	✓		
14				0	0	0		0	0		
15					0	0	X	X	0	0	0
16					0	0	0		0	0	0
17					✓	✓	✓	X	X	✓	✓
18						0	0	0		0	0
⋮											
21								✓	0	X	X

synchronous conditions, so that the stator at the rated current gives the maximum torque (i.e. with the armature reaction fundamental aligned with the q-axis)

Clearly, the amount of pull depends on several factors. First of all dimensional factors as machine diameters, gap width, magnets height, but also magnet coercive force and phase current. To make a coherent comparison across several machines with different slot – poles combinations, maintaining a feasible design, the following criteria have been adopted. The conductor current density, the magnets coercive force and the fundamental flux density amplitude had to be fixed depending on typical technical or physical constraints. Also the number of turns per tooth

and relative fill factor have been chosen to remain constant. The scaling of the other dimensional parameters is now explained.

The air gap flux density is the sum of the rotor and stator contributions and both are required to remain constant. The rotor flux density fundamental amplitude is proportional to pole pitch and average flux density, which depends on the ratio between magnet height (h_{mag}) and the magnetic gap (g_{mag}), comprising the air gap and the magnet height:

$$B_{Rp} \propto \frac{2\pi R_s}{p} \frac{h_{\text{mag}}}{g_{\text{mag}}} \quad (2.45)$$

As it is reasonable to maintain the ratios between stator radius and air gap for mechanical reasons and for magnetic consistence it is reasonable to maintain the ratio between air gap, magnetic gap and magnet height, R_s , h_{mag} and g_{mag} are kept proportional to p .

The stator flux density fundamental can be expressed as

$$\begin{aligned} B_{Sp} &= \mu_0 \frac{\bar{m}_p^\ominus}{g_{\text{mag}}} \\ &= \frac{\mu_0}{\pi} \frac{\kappa_{wp}^\ominus}{g_{\text{mag}} p} L N_{\text{tpp}} I_0 \end{aligned} \quad (2.46)$$

where N_{tpp} is the number of turns per phase, the total number of turns is $LN_{\text{tpp}} = ZN_t$ so

$$B_{Sp} = \frac{\mu_0}{\pi} \frac{\kappa_{wp}^\ominus}{g_{\text{mag}} p} I_0 Z N_t \quad (2.47)$$

which means that

$$\kappa_{wp}^\ominus I_0 Z N_t \propto g_{\text{mag}} p \quad (2.48)$$

So, being $g_{\text{mag}} \propto p$, we obtain

$$I_0 N_t \propto \frac{p^2}{\kappa_{wp}^\ominus Z} \quad (2.49)$$

The slot section (S_{slot}), for a given current density and fill factor, is proportional to the current and to the number of turns per tooth

$$S_{\text{slot}} \propto I_0 N_t \quad (2.50)$$

Which, substituting (2.49) becomes

$$S_{\text{slot}} \propto \frac{p^2}{\kappa_{\text{wp}}^{\ominus} Z} \quad (2.51)$$

Geometrically, the slot section is proportional to the slot height (h_{slot}) and to the slot pitch, which is proportional to the radius and inversely proportional to the number of slots

$$S_{\text{slot}} \propto h_{\text{slot}} \cdot \frac{R_s}{Z} \quad (2.52)$$

which solved for h_{slot} gives

$$\begin{aligned} h_{\text{slot}} &\propto \frac{S_{\text{slot}} Z}{R_s} \\ &\propto \frac{p^2}{\kappa_{\text{wp}}^{\ominus} Z} \frac{Z}{R_s} \\ &= \frac{p^2}{\kappa_{\text{wp}}^{\ominus} R_s} \end{aligned} \quad (2.53)$$

So, as $p \propto R_s$,

$$h_{\text{slot}} \propto \frac{R_s}{\kappa_{\text{wp}}^{\ominus}} \quad (2.54)$$

Finally, the electrical loading (A_i), which is the linear density of current distributed on the air gap, is defined as follows

$$\begin{aligned} A_i &= \frac{2N_t I_0}{R_s \tau_s} \\ &= \frac{2 \frac{p^2}{\kappa_{\text{wp}}^{\ominus} Z}}{R_s \frac{2\pi}{Z}} \\ &\propto \frac{p}{\kappa_{\text{wp}}^{\ominus}} \end{aligned} \quad (2.55)$$

which is proportional to p , as it is a common practice in the design of electrical machines [12].

So, once a machine is dimensioned for a certain configuration $Z - 2p$, a similar machine can be obtained scaling all dimensions proportionally to the number of poles except the slot height (which depends also on the winding factor) and the slot pitch (which depends also on the number of teeth).

Because in the machine scaling the average value of the flux density has been maintained, also the magnetic pressure has been maintained, so the magnetic pull force is expected to increase proportionally with the gap surface. As the proposed scaling does not involve the machine axial length (which has been arbitrarily kept to 0.1 m in the FEA simulations), the gap surface is proportional to R_s or also to p .

Based on the described model, for each configuration a sequence of FEA simulations has been done tracking the UMP for a complete turn (half electric period, as the UMP frequency is double of the electric frequency (2.38)). The average UMP has been subtracted to all values to obtain the dynamic pull excluding the static component, eventually the maximum was considered.

Table 2.7: Specific UMP, obtained for various $Z - 2p$ combinations, unconventional configurations are shaded, the conventional 21 – 16 is highlighted in yellow and ✓ indicates the configurations for which the UMP can be reduced.

$Z \backslash 2p$	2	4	6	8	10	12	14	16	18	20	22
3	1.67	4.52									
4	0.01		0.04								
5	0.07✓	2.64	2.87								
6		0		0							
7		0.68✓	3.28	2.08	1.13✓						
8		0	0		0						
9			0	3.96	1.65	0					
10			0	0		0	0				
11			0.87✓	0.83✓	4.62	1.34	0.35✓				
12				0	0		0	0			
13				0.38✓	0.22✓	5.28	1.1	1.0✓6	0.44✓		
14				0	0	0		0	0		
15					0	0	5.95	0.98	0	0	
16					0	0	0		0	0	0
17					0.31✓	0.48✓	0.13✓	6.59	0.82	0.06✓	0.24✓
18						0	0	0		0	0
⋮											
21								0.16✓	0	7.86	0.67

In Tab. 2.7, the resulting maximum pulls of all the cited $Z - 2p$ combinations have been collected, expressed as specific UMP [N/cm²] so that the effect of the scaling on the force is eliminated. The results of Tab. 2.7 confirm the evaluation of Tab. 2.6. The unconventional configurations are shaded and the ones for which the UMP is reducible are indicated by “✓”. The 21 – 16 UMP has been highlighted in yellow, this configuration has been chosen to demonstrate the application of the UMP minimization described in the following section.

2.5.3 Rotational symmetry

It is known that machines featuring a rotational symmetry are not affected by UMP [13]. This is intuitively explained by the consideration that if the module of the function representing the flux density has two or more periods along the air gap, the resulting forces will be similarly repeated along the air gap, resulting in a balanced set of forces.

This phenomenon can be seen also through the examination of the winding spectra. It has been demonstrated that a $Z - 2p$ configuration having UMP is characterized by a spectrum having neighbour harmonics different from zero. If a machine is built with a $kZ - k2p$ configuration, the resulting winding will be a $Z - 2p$ configuration repeated k times and the pull is balanced by the rotational symmetry. What happens in terms of spectrum is shown taking as an example the conventional configurations 5 – 4, 10 – 8 and 15 – 12.

It can be seen from Fig. 2.7 that every harmonic n is shifted to the position kn and the $k - 1$ harmonics separating them remain zero-valued. For this reason no harmonic can have a neighbour harmonic and therefore the UMP cannot arise.

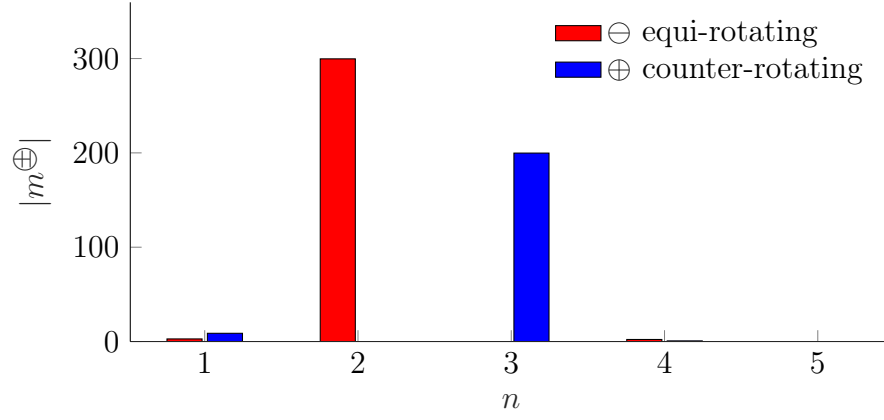
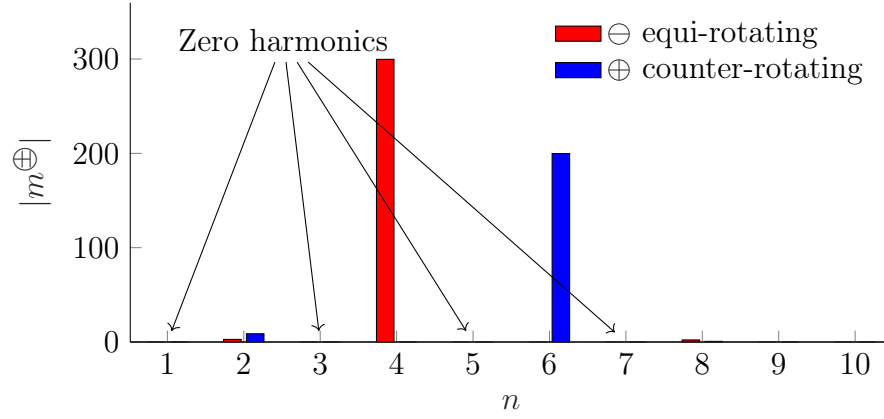
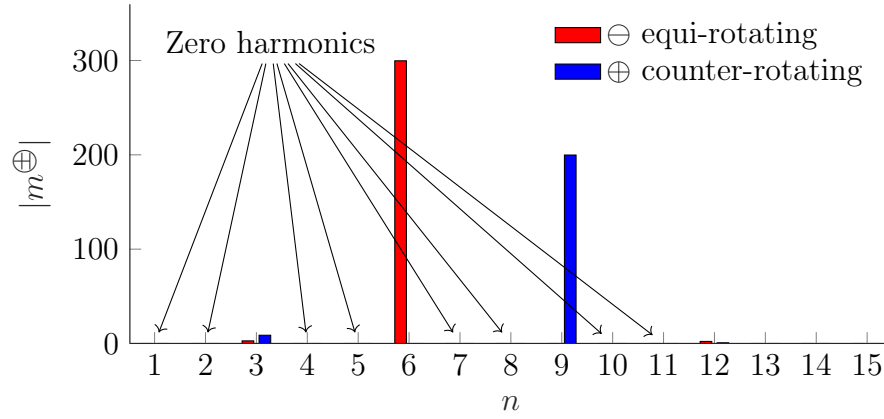
(a) $k = 1: 5 - 4$ (b) $k = 2: 10 - 8$ (c) $k = 3: 15 - 12$

FIGURE 2.7: Comparison between spectra of repeated configurations in order to achieve rotational symmetry

2.5.4 Application to a case study

As it can be seen in Tab. 2.7, there are many configurations for which the UMP is reducible, some of which having high UMP values, the first is the unconventional 5 – 2. Nevertheless, in order to demonstrate the procedure, a conventional configuration was preferred to underline the generality of the method, so the 21 – 16 configuration has been chosen even if it has a relatively low UMP.

The conventional winding for a 21 – 16 configuration can be obtained by the star of slots method. The principles of the machine design have been explained in section 2.5.2, (2.45) – (2.54); the resulting dimensions that have been used are referred to Fig. 2.8 and summarized in Tab. 2.8.

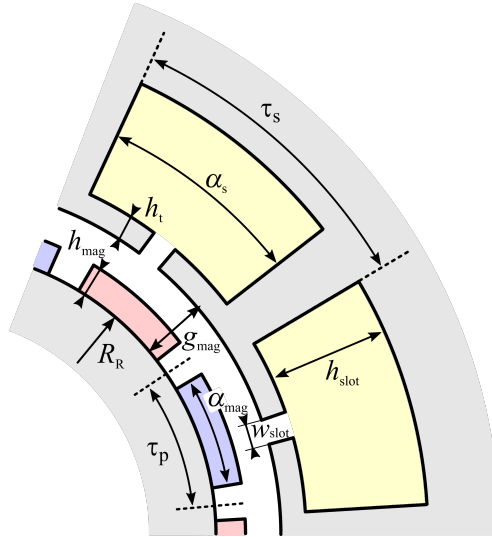
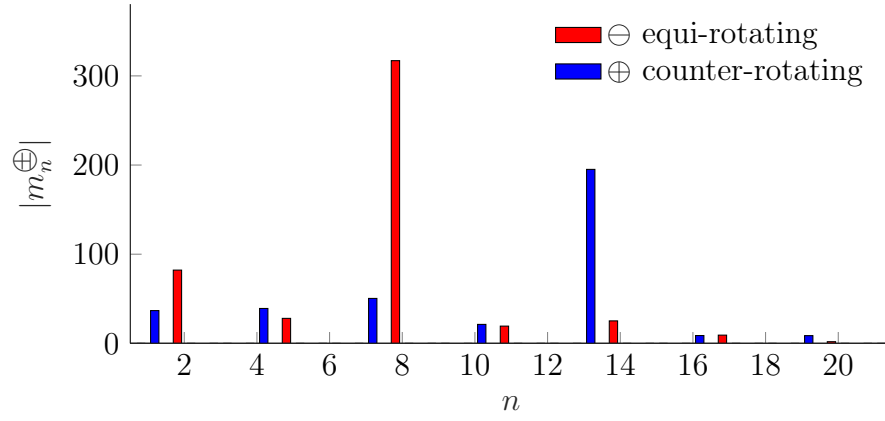


FIGURE 2.8: Data used for the 21 – 16 configuration FEA simulation

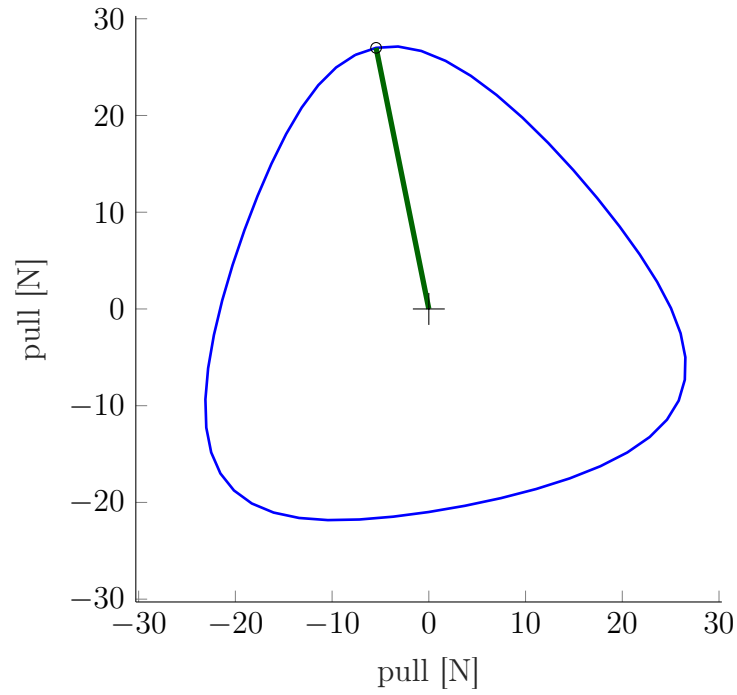
In Fig. 2.9a the spectrum of the winding is represented; the main UMP component is due to the fundamental harmonic (8^{th}) and the 7^{th} . Another relevant component of the pull is due to the 13^{th} – 14^{th} pair. From (1.36) it can be seen that the 13^{th} harmonic is linked to the 8^{th} , so it cannot be modified, but the 14^{th} is connected to the 7^{th} , which means that optimizing the winding in order to reduce the 7^{th} harmonic will necessarily reduce the 13^{th} harmonic too, therefore reducing both the UMP components simultaneously.

Table 2.8: Data used for the 21 – 16 configuration FEA simulation

Symbol	definition	value
R_R	rotor iron radius	132 mm
h_{mag}	magnet height	24 mm
g_{mag}	magnetic air gap	28 mm
h_t	lip height	2.5 mm
h_{slot}	slot height	80 mm
α_{slot}	slot angular amplitude	0.133 rad
α_{mag}	magnet angular amplitude	0.284 rad
w_{slot}	slot opening	2 mm
I_0	current peak value	4.27 A



(a) Harmonic spectrum



(b) UMP force vector trajectory, the maximum pull is indicated by the green line.

FIGURE 2.9: Spectrum and pull trajectory of a star-of-slots winding applied to 21 – 16 configuration

In Fig. 2.9b, the trajectory of the force vector of the magnetic pull is represented. It can be seen that the UMP does not have a constant module. This is due to the presence of pull due to other harmonics. The instant in which the maximum value of the force is reached is represented by the green line.

In order to reduce the pull, the objective function relative to the 7th harmonic can be obtained from (2.23) using only \mathbf{Q}_7^\oplus . The minimum fundamental lower bound is not a linear constraint, so it is treated (as seen in 2.4) with a sequence of linearly constrained optimizations using (2.33) together with the constraints deriving from (2.20).

$$\mathfrak{F}_{\min 7^{\text{th}}}(\mathbf{w}) = \mathbf{w}^T \mathbf{Q}_7^\oplus \mathbf{w} \quad (2.56a)$$

$$\text{LB} < [\cos(\alpha) \text{Re}(\bar{\mathbf{v}}_p^\ominus) + \sin(\alpha) \text{Im}(\bar{\mathbf{v}}_p^\ominus)] \mathbf{w} \quad (2.56b)$$

A quasi-optimum is obtained from the minimum among all the minima obtained varying α .

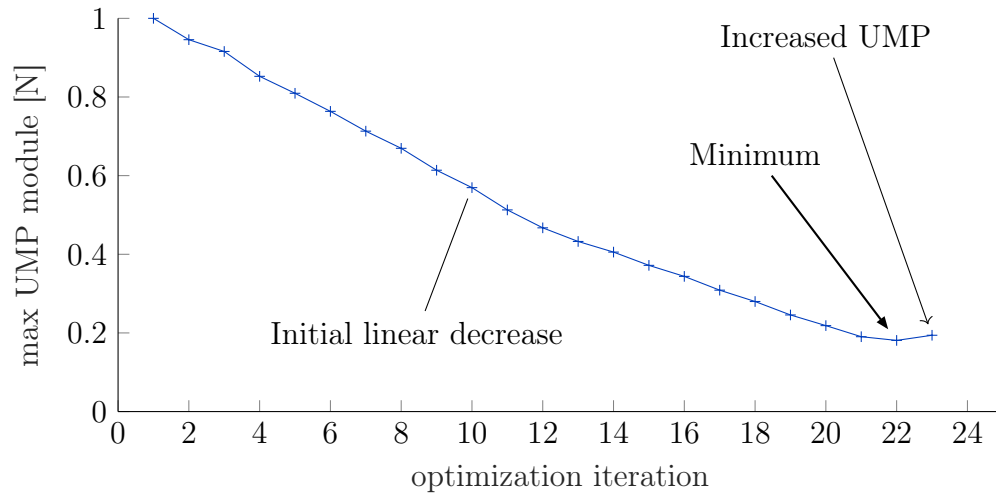


FIGURE 2.10: UMP relative variation iterating the 7th harmonic minimization. in abscissa the iteration step, corresponding to a fundamental decrease of 0.1%

A sequence of simulations has been performed using the increasingly optimized windings obtained minimizing the 7th harmonic, while decreasing the fundamental lower bound. The results are summarized in Fig. 2.10. The UMP is represented relative to its maximum value,

corresponding to the conventional configuration. For every step, the optimization has been made decreasing the fundamental lower bound by 0.1%, which means that the lowest UMP value is reached decreasing the fundamental by 2.2%.

Each of the points in Fig. 2.10 has been obtained extracting the maximum UMP from a sequence of simulations made to obtain the UMP for every angular position of the rotor. In Fig. 2.11 the whole trajectories of the relative UMP are shown for a selection of indexes. The UMP direction in which the maximum module is reached is highlighted for every case. While the UMP due to the 7th harmonic decreases, the contribution of the residual harmonics becomes more and more evident.

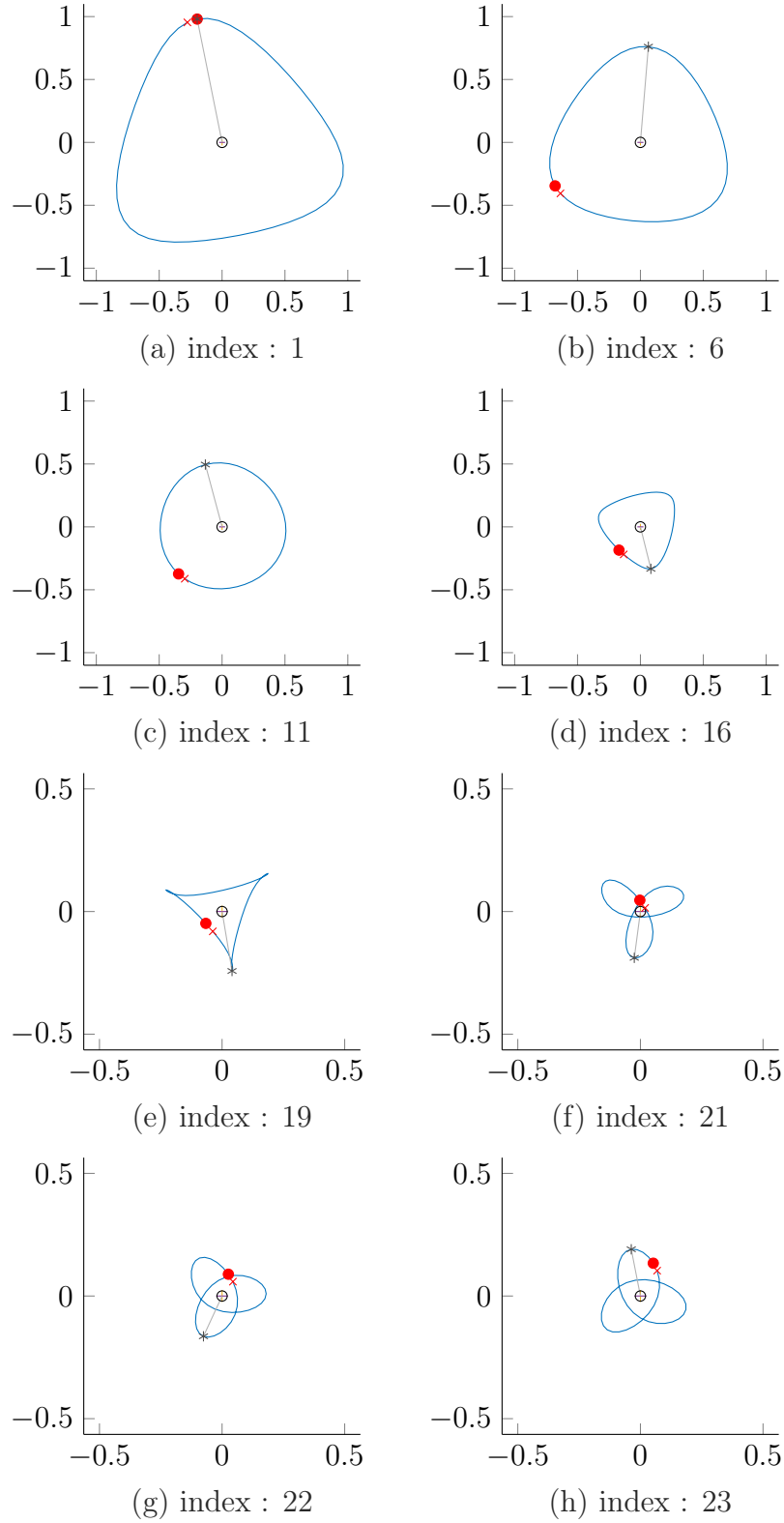


FIGURE 2.11: Relative UMP trajectories for a selection of indexes. The axes scales have been modified in accordance to the UMP module

A comparison between the star of slots spectrum and the one with the minimized 7th harmonic is shown in Fig. 2.12. The highest harmonic peaks (8 and 13) are linked and the neighbour harmonics causing UMP are the 7th and the 14th respectively. The reduction of the 7th harmonic is evident, and also the linked 14th harmonic (near the 13th) is proportionally reduced as expected. By the way it can be noticed that other harmonics grow to such an extent (see the orange marking) that reducing further the 7th harmonic increases the UMP because the other contributions have become predominant. This justifies the fact that the last value in Fig. 2.10, is slightly higher than the previous.

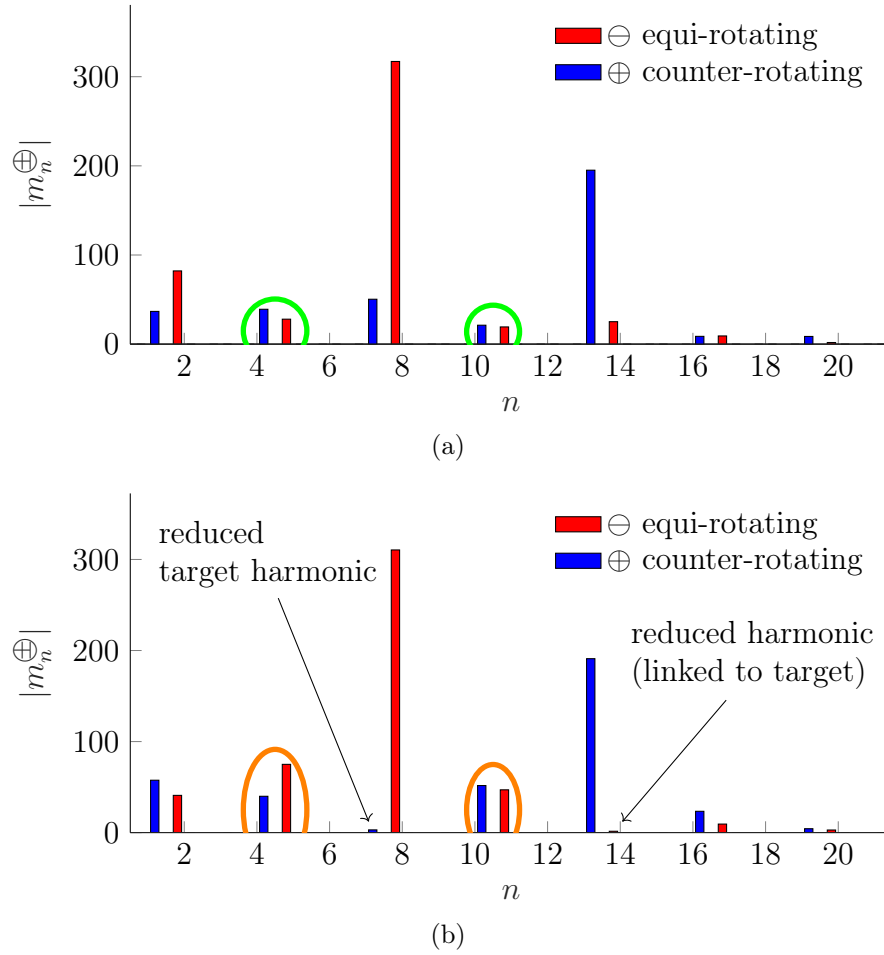


FIGURE 2.12: Comparison between (a) star-of-slots and (b) optimized 21 – 16 configuration spectrum, the increased harmonics are highlighted by the marking changing from green to orange

References

- [1] A. Tassarolo. “A Quadratic-Programming Approach to the Design Optimization of Fractional-Slot Concentrated Windings for Surface Permanent-Magnet Machines”. In: *IEEE Transactions on Energy Conversion* 33.1 (Mar. 2018), pp. 442–452. ISSN: 0885-8969. DOI: 10.1109/TEC.2017.2751588. URL: <https://ieeexplore.ieee.org/document/8031978/>.
- [2] Alexander Gray and J. G. Pertsch. “Critical Review of the Bibliography on Unbalanced Magnetic Pull in Dynamo-Electric Machines”. In: *Transactions of the American Institute of Electrical Engineers* XXXVII.2 (July 1918), pp. 1417–1424. ISSN: 0096-3860. DOI: 10.1109/T-AIEE.1918.4765577. URL: <http://ieeexplore.ieee.org/document/4765577/>.
- [3] R. C. Robinson. “The Calculation of Unbalanced Magnetic Pull in Synchronous and Induction Motors”. In: *Transactions of the American Institute of Electrical Engineers* 62.10 (Oct. 1943), pp. 620–624. ISSN: 0096-3860. DOI: 10.1109/T-AIEE.1943.5058614. URL: <http://ieeexplore.ieee.org/document/5058614/>.
- [4] Ahmad A. Salah, David G. Dorrell, and Youguang Guo. “A Review of the Monitoring and Damping Unbalanced Magnetic Pull in Induction Machines Due to Rotor Eccentricity”. In: *IEEE Transactions on Industry Applications* 55.3 (May 2019), pp. 2569–2580. ISSN: 0093-9994. DOI: 10.1109/TIA.2019.2892359. URL: <https://ieeexplore.ieee.org/document/8607021/>.
- [5] K.J. Binns and M. Dye. “Identification of principal factors causing unbalanced magnetic pull in cage induction motors”. In: *Proceedings of the Institution of Electrical Engineers* 120.3 (1973), p. 349. ISSN: 00203270. DOI: 10.1049/piee.1973.0072. URL: <https://digital-library.theiet.org/content/journals/10.1049/piee.1973.0072>.
- [6] J. Y. Song et al. “Cogging Torque and Unbalanced Magnetic Pull Due to Simultaneous Existence of Dynamic and Static Eccentricities and Uneven Magnetization in Permanent Magnet Motors”. In: *IEEE Transactions on Magnetics* 53.3 (2016), pp. 1–1. ISSN: 0018-9464. DOI: 10.1109/TMAG.2016.2628098. URL: <http://ieeexplore.ieee.org/document/7742931/>.
- [7] P. Pennacchi and L. Frosini. “Dynamical behaviour of a three-phase generator due to unbalanced magnetic pull”. In: *IEE Proceedings - Electric Power Applications* 152.6 (2005), p. 1389. ISSN: 13502352. DOI: 10.1049/

- ip-epa:20050178. URL: https://digital-library.theiet.org/content/journals/10.1049/ip-epa%7B%5C_%7D20050178.
- [8] E. Sarani, K. Abbaszadeh, and M. Ardebili. “Modeling and simulation of turn-fault and unbalance magnetic pull in induction motor based on magnetic equivalent circuit method”. In: *2005 International Conference on Electrical Machines and Systems*. Vol. 1. 8. IEEE, 2005, 52–56 Vol. 1. ISBN: 7-5062-7407-8. DOI: 10.1109/ICEMS.2005.202482. URL: <http://ieeexplore.ieee.org/document/1574715/>.
- [9] K. J. Meessen, J. J. H. Paulides, and E. A. Lomonova. “Force Calculations in 3-D Cylindrical Structures Using Fourier Analysis and the Maxwell Stress Tensor”. In: *IEEE Transactions on Magnetics* 49.1 (Jan. 2013), pp. 536–545. ISSN: 0018-9464. DOI: 10.1109/TMAG.2012.2206821. URL: <http://ieeexplore.ieee.org/document/6228537/>.
- [10] Z. Q. Zhu et al. “Unbalanced Magnetic Forces in Permanent-Magnet Brushless Machines With Diametrically Asymmetric Phase Windings”. In: *IEEE Transactions on Industry Applications* 43.6 (2007), pp. 1544–1553. ISSN: 0093-9994. DOI: 10.1109/TIA.2007.908158. URL: <http://ieeexplore.ieee.org/document/4385010/>.
- [11] D.G. Dorrell and A.C. Smith. “Calculation of UMP in induction motors with series or parallel winding connections”. In: *IEEE Transactions on Energy Conversion* 9.2 (June 1994), pp. 304–310. ISSN: 08858969. DOI: 10.1109/60.300144. URL: <http://ieeexplore.ieee.org/document/300144/>.
- [12] Valeria Hrabovcova Juha Pyrhonen Tapani Jokinen. *Design of Rotating Electrical Machines*. 2nd ed. Wiley, Dec. 2013. ISBN: 978-1-118-58157-5.
- [13] G.H. Jang et al. “Torque and unbalanced magnetic force in a rotational unsymmetric brushless DC motors”. In: *IEEE Transactions on Magnetics* 32.5 (1996), pp. 5157–5159. ISSN: 00189464. DOI: 10.1109/20.539522. URL: <http://ieeexplore.ieee.org/document/539522/>.

Chapter 3

Study and implementation of an unconventional FSCW

The study on unconventional FSCW windings has been applied to an innovative machine designed to be both a motor and a generator for sailing boats. The particular application and the environmental conditions determined a set of requirements that were frequently in contrast and hard to meet.

The core of the machine is a hub-less, high efficiency propeller designed for 1000 rpm at cruising speed of 8 kts (i.e. about 4 m/s) with an internal diameter of 400 mm and a rated power of 15 kW. A concept design is shown Fig. 3.1

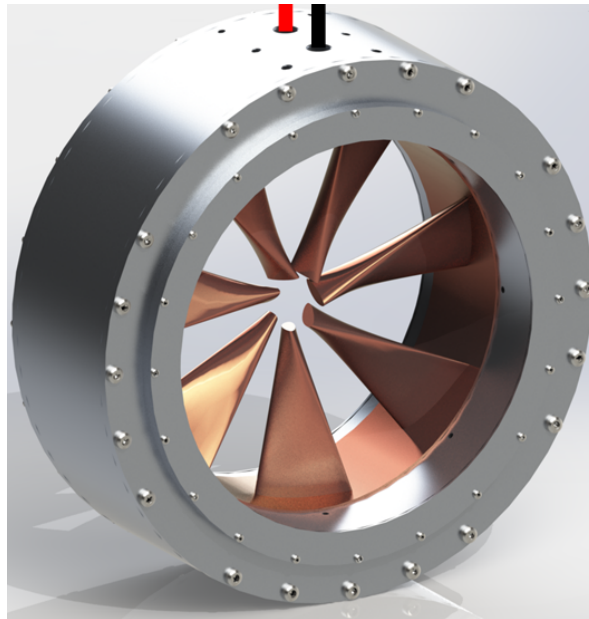


FIGURE 3.1: Concept design of the sailing boat hub-less motor-generator

3.1 Machine specifications and requirements

The hub-less propeller is a ducted propeller with the blades attached to a rotating duct. While the hub-less design, if compared to the conventional design, granted a higher fluid-dynamic efficiency to the propeller, the design of the electrical machine was strongly conditioned by the performance requirements leading to geometrical, mechanical and electrical constraints.

First, to eliminate any mechanical couplings that would bring friction losses and vibrations, a direct coupling was required. As the propeller has a hub-less design, the only solution was a “rim motor”: instead of having a conventional motor connected to the propeller through a shaft, the electrical machine in this case occupies the circumferential area around the propeller that is housed inside the rotor.

Second, to reduce the hydro-dynamic drag due to the motor section as much as possible, the radial dimension of the machine has been constrained to be less than 100 mm including the propeller duct, the rotor, the stator and the outer frame. Because of the high ratio between the machine diameter and the sections of the stator and the rotor, the rigidity could become a critical issue, so the mechanical gap had to be wide enough to guarantee no contact between the two parts in case of deformation. In fact, at the same time the whole structure may be subject to the thrust of the propeller, the drag of the stator section, to vibrations, to the impact of debris, and to magnetic forces, especially if part of the machine is deactivated for a fault.

Finally, the machine was required to be self-contained, meaning that it had to be connected only to the 12 V – DC shipboard system and the converter had to be internal to the structure.

3.2 Rotor

A wide mechanical gap excluded the option of an induction machine that would have required an excessive magnetizing current, impacting negatively on the efficiency or on the dimensions of the converter and the winding. A wound rotor synchronous machine has not even been considered because of the difficulty to connect the rotor field circuit, in

sea water and with no shaft. So finally, a PM solution looked both the most efficient and easily implementable. Between an IPM and an SPM design, the SPM was preferred because any Internal Permanent Magnet (IPM) design would have required a higher radial dimension and more weight.

The requirement of a high efficiency leads on one hand to reduce the radial dimension of the machine, that can be obtained increasing the number of poles, but on the other hand an increase of the number of poles increases the working frequency and therefore the iron losses. A limit had to be established at a rated frequency 200 Hz, so the number of pole pairs (p) was calculated as

$$p = \frac{60 f}{n} = \frac{60 \cdot 200}{1000} = 12 \quad (3.1)$$

where f indicates the maximum frequency and n the rated rotation speed expressed in rpm. The choice of 24 poles allowed for a radial dimension of the yokes of 10 mm which is also a mechanical limit for the machine rigidity. The rotor layout is shown in Fig. 3.2

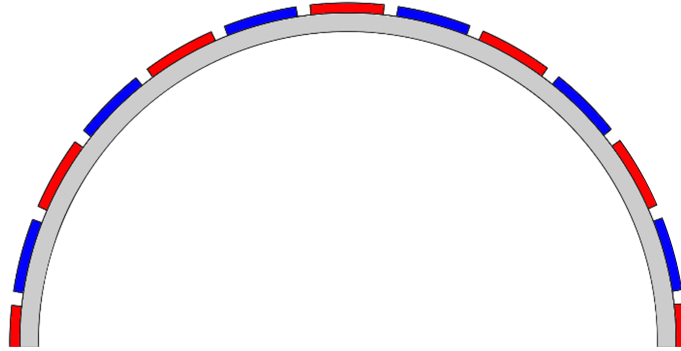


FIGURE 3.2: Half section of the 24 poles rotor

3.3 Stator

In order to achieve a certain degree of fault tolerance, the stator was required to be divided into sections, so that if a fault leads to deactivate one section, the others continue operating. To maintain a balance in the magnetic forces between stator and rotor, if a section is deactivated, another diametrically opposite one, must be deactivated too, in order to preserve the rotational symmetry. For this reason the sections had to

organized in pairs and an odd number of sections is excluded. In order to meet the fault tolerance requirement, the lowest number of section pairs was two, so a total of four sections.

In its final design (Fig. 3.3), the machine consists of four independent three-phase sections, each connected to an AC/DC converter fed by the 12 V – DC shipboard system. Also the power required from the single AC/DC converter is reduced by a factor of four, reducing its dimensions. This aspect was particularly important because it was specifically required to house the converters in the machine frame.

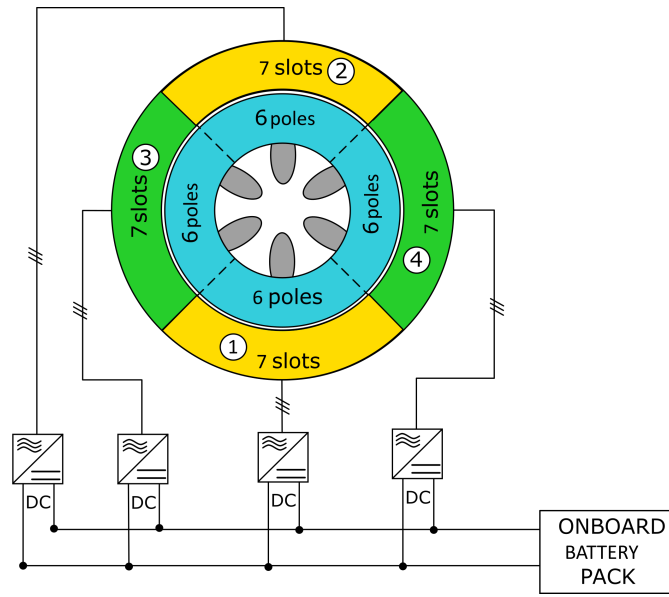


FIGURE 3.3: Schematic of the four sections of the machine fed by the four converters

When the machine is operated as a generator, a low torque and power may be available. Clearly in this case a high efficiency is particularly important, but also a low cogging torque is required, both to start the machine passively and because the cogging torque would lead to an undesirable torque ripple, which has to be avoided so that the propeller can run fluidly at constant speed and no vibrations are produced.

The cogging torque is proportional to the greatest common divisor (gcd) between Z and $2p$. As it can be easily seen by [1], where the torque is stated to be proportional to C_T , with

$$C_T = \frac{Z \cdot 2p}{\text{LCM}(Z, 2p)} = \text{gcd}(Z, 2p) \quad (3.2)$$

where LCM denotes the least common multiple. Clearly the best choice from this point of view would be a configuration for which Z and $2p$ are co-prime numbers, so that C_T takes its minimum value (i.e. 1).

Because the stator has been divided into four sections, each section works as a 6-poles machine. From table Tab. 2.4 we can see that a conventional $Z - 2p$ configuration having 6 poles would be the $9 - 6$, having a $C_T = 3$, a winding factor $\kappa_w = 0.866$ and magnet specific losses (0.16 mW/mm^3 , from Tab. 2.5). From the first table we can see that the highest winding factor is obtained with a 7-teeth-per-section stator ($\kappa_w = 0.918$, $7 - 6$ configuration), which has a value of $C_T = 1$, even though the losses are a little higher (0.55 mW/mm^3), but still below the acceptable limits. In this case the UMP is not a concern because the machine has a rotational symmetry (see section 2.5.3). So, finally, a 28 teeth stator has been chosen, shown in Fig. 3.4.

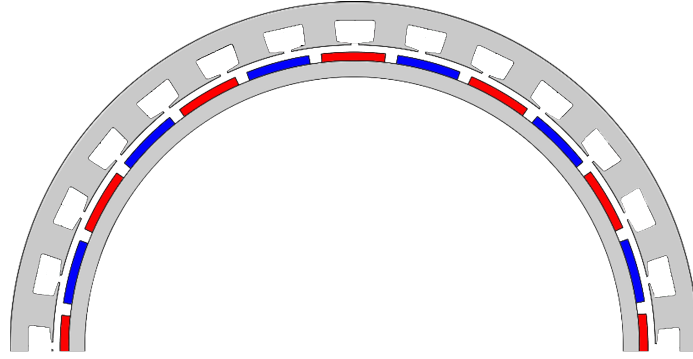


FIGURE 3.4: Half section of the 24 poles rotor coupled with the 28 teeth stator

For the chosen configuration ($28 - 24$) a test on the cogging torque has been done by FEA analysis (Fig. 3.5), the maximum value was below 0.5 Nm .

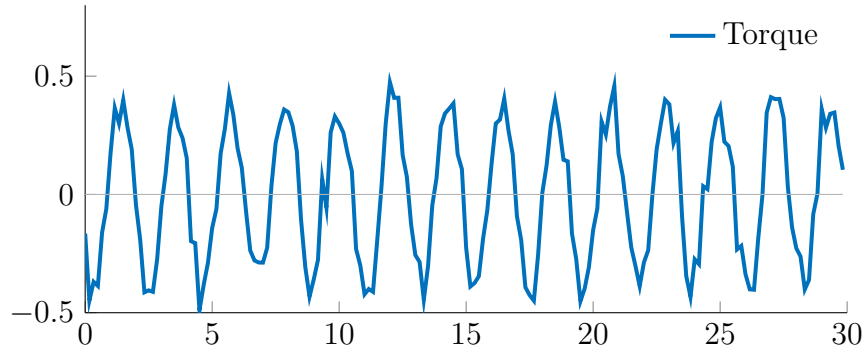


FIGURE 3.5: Cogging torque obtained by FEA simulation on the 28 – 24 configuration

3.4 Unconventional FSCW choice

To obtain the winding layout, a two step optimization has been done. As a first step, using the constraints $\mathfrak{C}(\mathbf{w})$ given by (2.20) and shown below, the winding vector (\mathbf{w}_1) was obtained from the objective function (3.3) that maximizes the fundamental

$$\mathfrak{C}(\mathbf{w}) = \begin{cases} \mathbf{A}_0 \mathbf{w} & \leq \mathbf{0}_{2LZ} \\ \mathbf{A}_T \mathbf{w} & \leq N_t \cdot \mathbf{1}_Z \\ \bar{\mathbf{A}}_S \mathbf{w} & = 0 \end{cases}$$

$$\mathfrak{F}_{\text{fund}}(\mathbf{w}) = -\mathbf{w}^T \mathbf{Q}_3^\ominus \mathbf{w} \quad (3.3)$$

In the second step, the losses are minimized (3.4a), while, together with $\mathfrak{C}(\mathbf{w})$, the maximum module of the fundamental has been imposed as a lower bound (3.4b).

$$\mathfrak{F}_{\text{loss}}(\mathbf{w}) = \mathbf{w}^T \mathbf{Q}_{\text{harm}} \mathbf{w} \quad (3.4a)$$

$$\text{LB} < [\cos(\alpha) \text{Re}(\mathbf{v}_p^\ominus) + \sin(\alpha) \text{Im}(\mathbf{v}_p^\ominus)] \mathbf{w}_1 \quad (3.4b)$$

The winding obtained from the optimization has been rounded and the correspondent winding matrix is shown in Tab. 3.1.

Table 3.1: Winding matrix used for each 7 – 6 section of the 28 – 24 configuration, $N_t = 60$.

$k \backslash l$	0	1	2	3	4	5
0	0	60	0	0	0	0
1	0	0	0	20	40	0
2	60	0	0	0	0	0
3	0	0	7	53	0	0
4	7	0	0	0	0	53
5	0	0	60	0	0	0
6	0	0	0	0	40	20

So, finally, Fig. 3.6 shows the winding layout of the 28 – 24 machine (only half the complete machine is shown). In Fig. 3.7 the spectrum corresponding to the complete machine is shown.

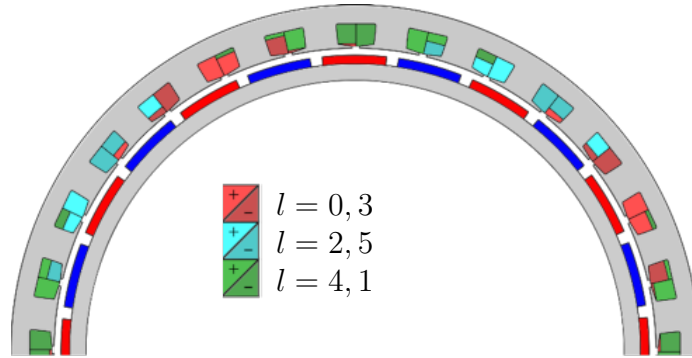


FIGURE 3.6: Half section of the 28 – 24 configuration with the winding representation

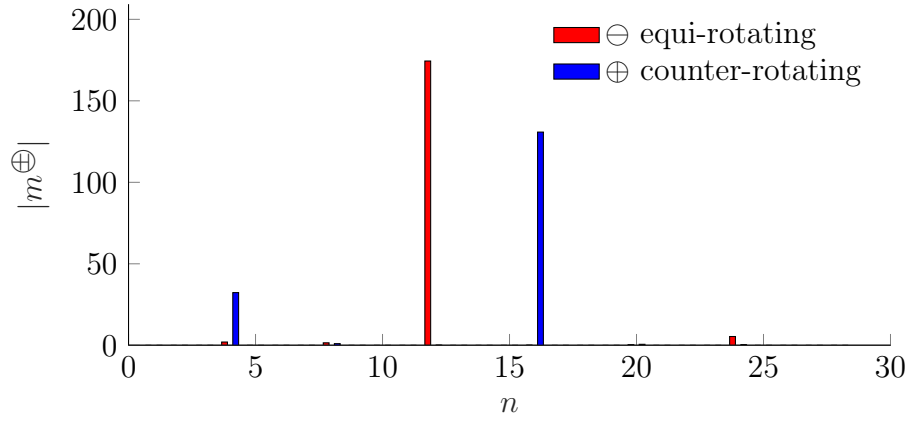


FIGURE 3.7: Amplitude of the harmonics for the 28 – 24 configuration, in red the harmonics rotating anticlockwise as the fundamental, in blue the harmonics rotating clockwise.

In Fig. 3.7, the characteristics of a repeated configuration is confirmed (see section 2.5.3, the 28 – 24 is obtained by a 7 – 6 repeated 4 times): the harmonics different from 0 are separated by three zero-valued harmonics, therefore no UMP is generated.

Once the configuration was decided, in order to optimize the machine dimensions, a set of FEA simulations has been done to refine the design, so that the radial dimensions were minimized while maintaining a sufficient slot section to avoid excessive current density and a sufficient yoke section for the structural rigidity and to avoid saturation.

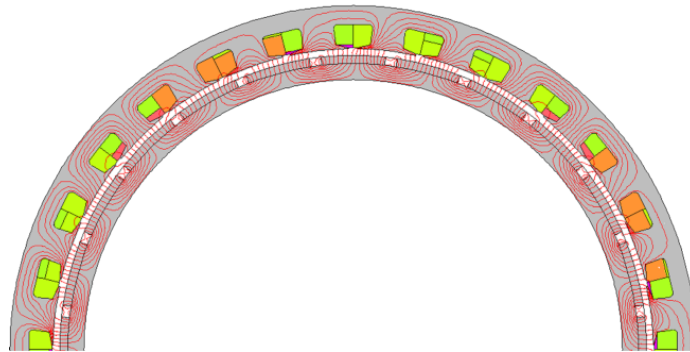


FIGURE 3.8: Half section of the 28 – 24 configuration. the winding colours are related to the current density, the flux lines are represented in red

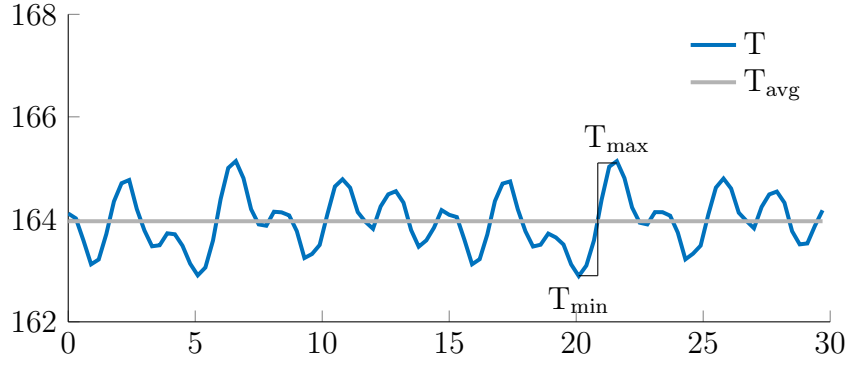


FIGURE 3.9: Torque obtained by a 15A FEA simulation on the 28 – 24 configuration

For the chosen configuration, the torque ripple obtained was obtained by FEA simulation (Fig. 3.9) is and calculated in (3.5) where T_{\max} , T_{\min} and T_{avg} represent respectively maximum, minimum and average torque:

$$T_{\text{rip}} = \frac{T_{\max} - T_{\min}}{T_{\text{avg}}} = 1.4\% \quad (3.5)$$

while the one obtained for the conventional winding 36 – 24 was 14.8%

3.5 Mechanical design

The mechanical design has been developed after making several considerations and after evaluating several options.

The first consideration was if the sea water was to enter the structure. The choice was free at the beginning, because on one hand the losses did not require an internal water flux to dissipate the heat, as the dissipation through the immersed frame was widely sufficient. On the other hand, because the entrance of some water could not be excluded in any condition, all the active parts had to be insulated with resin anyway.

The first option was to use plastic material sleeve bearings lubricated and refrigerated by sea water (see Fig. 3.10). The sleeve bearings had to be mounted between the rotor frame structure and a shield mounted on the stator frame.

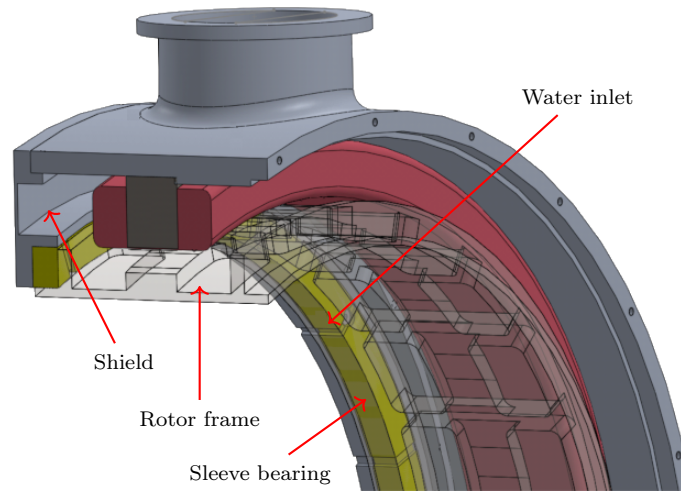


FIGURE 3.10: Section of the sleeved machine the sleeve is highlighted in yellow

This solution would have let in at least the amount of water necessary to lubricate the sleeve bearings, filling the machine. Because the drag caused by any turbulence in the gap was hardly predictable and because the water remaining in the motor on the long term may cause the growth of marine organisms, it was finally decided to prevent the water entrance.

A second option was to use ball bearings coupled with a hydraulic sealing 3.11.

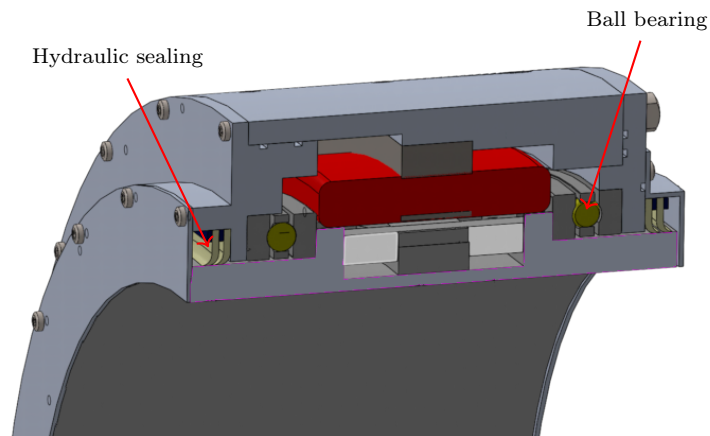


FIGURE 3.11: Second design of the machine the ball bearing and the hydraulic sealing are shown

In this case the ball bearing solution seemed optimal. The size of the ball bearing that can be seen in Fig. 3.11 is taken from a catalogue and the loads and materials were suitable for the seawater environment.

Unfortunately it was not available for purchase and the available ones were not fit for the application as they were far too big, weighing 25kg each.

The final design substituted the ball bearing with a series of cam rollers fixed to the rotor frame and running on a track fixed to the stator frame. The front and rear tracks have an angle so that they can react both to radial and axial forces.

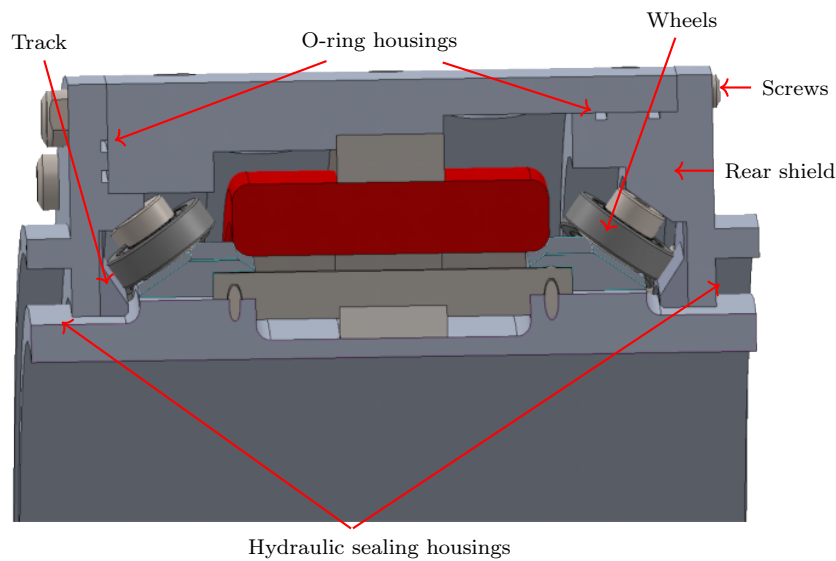


FIGURE 3.12: Section of the final machine with the cam rollers

The shields include the housings of sealing O-rings. The rear shield is designed so that tightening the screws, the sealing lets the shield free to slide forward. In this way the radial mechanical slack between the wheels and the tracks can be absorbed and the correct pressure can be applied to the tracks.

Some more particulars of the construction can be seen in Fig. 3.13, in particular, the ferromagnetic inter-magnets and the threaded holes for the propeller can be seen. The ferromagnetic inter-magnets, in addition to a higher structural rigidity, give the rotor a magnetic anisotropy that is required by the sensor-less control system. The internal threaded holes were used both for the propeller and to fix the machine to the test bench.

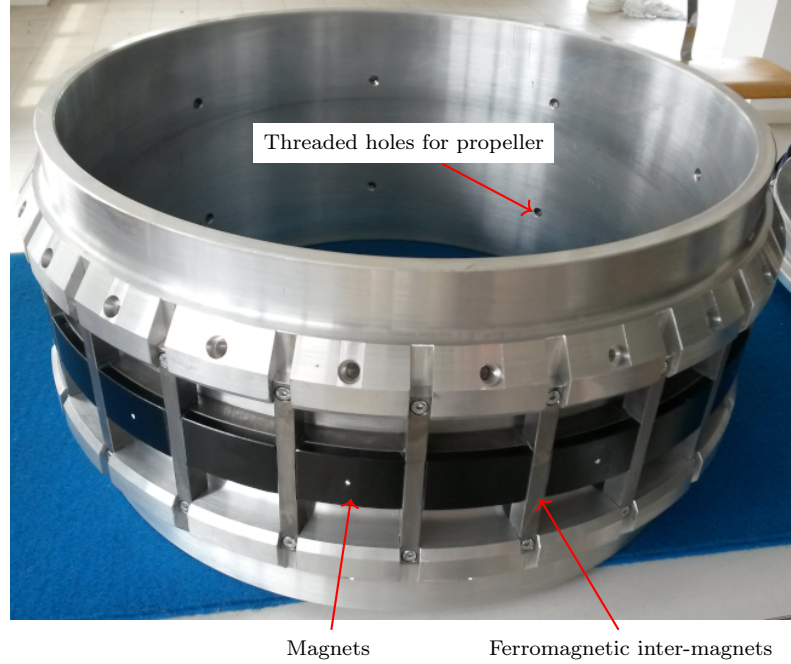


FIGURE 3.13: Rotor of the prototype

3.6 Measurements

During the design stage, each design was tested through FEA simulationsto assess the prototype performance and to establish the final dimensions. For the final design and the alternative designs considered earlier with different slot – poles combinations, the simulations showed that the FSCW windings did not introduce any kind of unexpected parasitic phenomenon such as eddy current losses in non-active parts.

In order to achieve an experimental validation of FEA time-stepping simulations, the results are compared to the laboratory test bench measurements.

The tests have been performed on the machine operating in generator mode, on two diametrically opposite sections connected in parallel on an RL load or to a diode rectifier feeding a resistor (Fig. 3.15). The other two sections were left at open circuit.

In the test conducted with the RL load, the load is composed of three star-connected RL loads (Fig. 3.15a), while in the arrangement depicted in (Fig. 3.15b) the load consists of a diode rectifier connected to a resistive load. The voltages and currents measured on each phase in the two test arrangements at 50 Hz are shown in Fig. 3.16a and Fig. 3.16b.

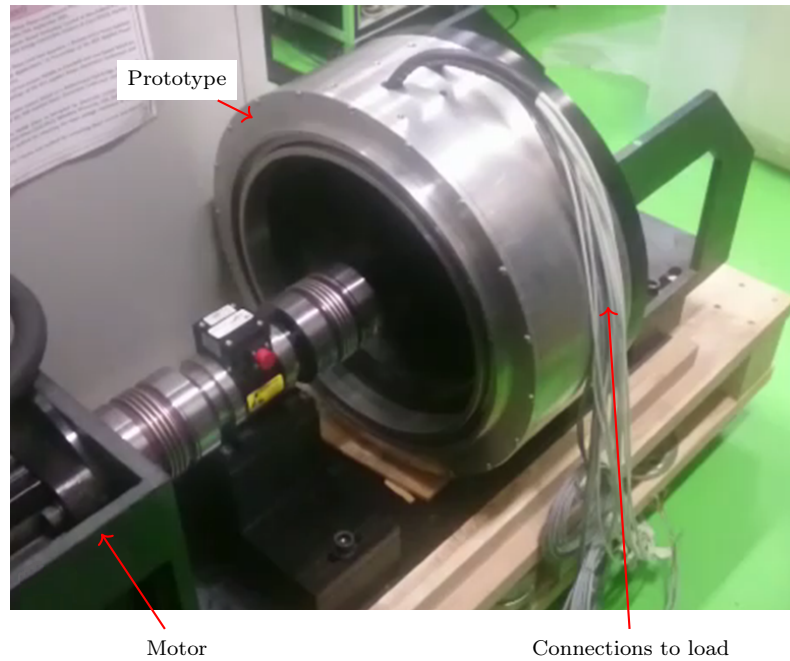


FIGURE 3.14: Rotor of the prototype

It can be seen that the machine, although loaded on only two of its four sectors, exhibits the same balanced symmetrical behaviour that would be expected in case of a conventional FSCW winding.

The tests have been repeated exchanging the sections (4 and 2 connected, 1 and 3 left open) and, as expected, the same voltage and current waveforms shown in Fig. 3.16 have been obtained under the same load conditions.

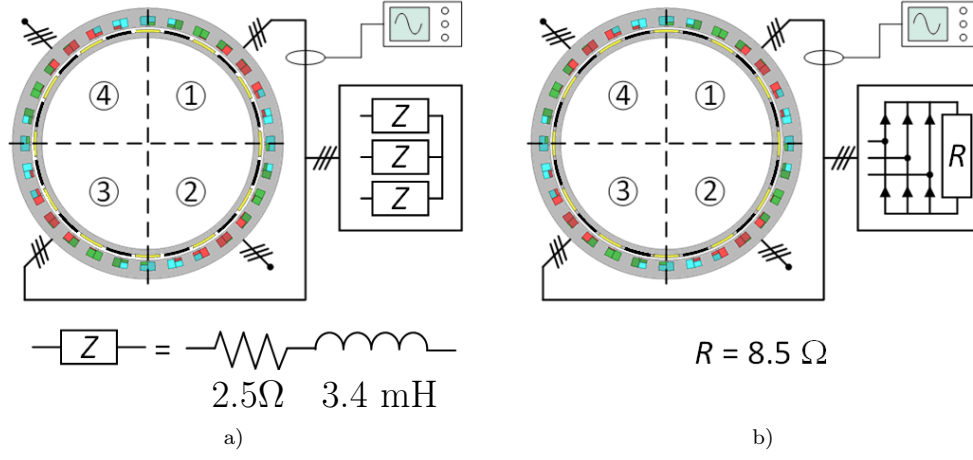


FIGURE 3.15: Test setup

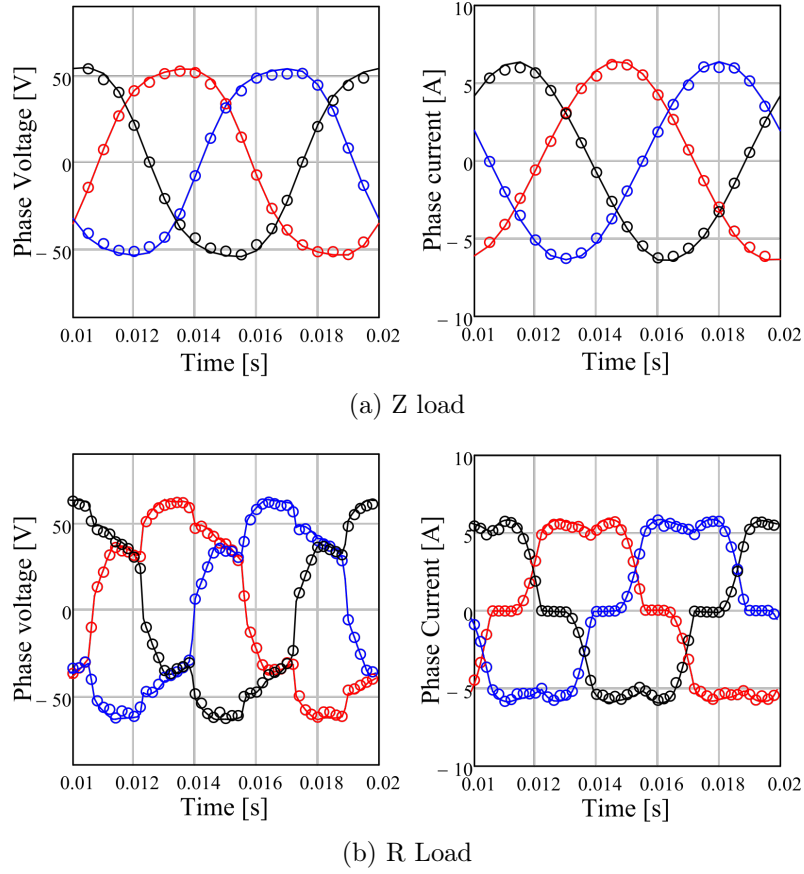


FIGURE 3.16: Comparison:
 ○ ○ ○ test measurements — FEA simulation

Conclusion

In this dissertation an analysis, optimization and extension of the Fractional Slot Concentrated Windings design has been proposed. In particular, after developing a mathematical framework to model multi-phase multi-layer FSCW windings and the produced harmonic content, it has been shown that there are a number of independent harmonics equal to the number of teeth and all the other harmonics are linearly dependent on them. This structural constraint affects any winding independently of number of phases and winding topology.

After this, the design of the winding topology has been approached as an optimization problem applied to the winding topology. As a part of the study, it has been shown how FSCWs can be designed with “unconventional” slot-pole configurations that are regarded as unfeasible if the star of slots is used.

The first step was to obtain symmetric windings with the highest possible fundamental. It has been shown that, for any slot-poles configuration, the winding topology can be obtained by quadratic optimization of the fundamental amplitude and the symmetry of the winding can be imposed as a linear constraint. The resulting windings for unconventional configurations feature analogous performance to conventional windings and conventional windings obtained by optimization coincide with the ones obtained by the star of slots.

As a second step, it has been shown that quadratic maximization can be also used to reduce the losses in the magnets, which corresponds to suitably reducing all harmonics other than the fundamental. The effectiveness and usefulness of the method has been proven. As an example the conventional 9-slot – 8-pole configuration, has shown a reduction of losses by 25.8%, accepting reduction of the fundamental by 2%.

A third step has been to analyse the relationship between harmonic content and UMP. Again it has been demonstrated that the winding can be optimized in order to reduce the specific harmonics responsible

for the UMP. Based on the harmonic content, a simple criterion has been given to identify the slot-pole configurations for which the UMP can be optimised. While it has been shown that in many cases the UMP reduction is not necessary or not possible (because the harmonics responsible for the UMP are linked to the fundamental), a conventional configuration has been chosen among the optimizable ones as a case study to test the method effectiveness. In this case the UMP was reduced to 18% accepting a reduction of the fundamental by only 2.2%.

Finally, an application in which the unconventional FSCW has been used has been presented. The manufacturing the prototype and the test results have confirmed the feasibility of the winding and the performance expected from FEA simulation.

As a conclusion it can be said that unconventional windings extend noticeably the amount of configurations available for the designer with no drawbacks. Furthermore, the same technique used to design the unconventional configuration windings can be used to optimize the conventional windings obtained by the star-of-slots to reduce losses or UMP.